



Contents lists available at ScienceDirect

International Journal of Solids and Structures

journal homepage: www.elsevier.com/locate/ijsolstrLoss of ellipticity analysis in non-smooth plasticity[☆]B. Staber^{a,*}, S. Forest^b, M. Al Kotob^c, M. Mazière^b, T. Rose^a^a Safran Tech, Modeling and Simulation, Rue des Jeunes Bois, 78114 Magny-Les-Hameaux, France^b MINES ParisTech, PSL University, Centre des matériaux, CNRS UMR 7633, BP 87 91003 Evry, France^c Safran Aircraft Engines Villaroche, Rond Point René Ravaud-Réau, 77550 Moissy-Cramayel, France

ARTICLE INFO

Article history:

Received 27 October 2020

Received in revised form 28 January 2021

Accepted 22 February 2021

Available online 10 March 2021

Keywords:

Loss of ellipticity

Rice's criterion

Localization

Non-smooth yield functions

Corners

Critical hardening modulus

Tresca

ABSTRACT

This work is concerned with the influence of non-smooth yield functions on material instabilities. The loss of ellipticity condition is examined in the case of a family of non-smooth yield functions in principal stress space. A procedure for the numerical detection of loss of ellipticity in multisurface plasticity is proposed. An explicit expression of the subdifferential of the non-smooth yield function is obtained, thereby extending existing results in the literature for the Tresca and Mohr–Coulomb criteria. Structural computations show that the use of non-smooth yield functions can lead to much earlier failure prediction than in the case of a commonly used von Mises criterion.

© 2021 Elsevier Ltd. All rights reserved.

1. Introduction

This work is concerned with strain localization in the context of non-smooth plasticity. Introduced by Hill (1962) and Rice (1976), loss of ellipticity is commonly used as a criterion for the detection of the onset of strain localization. Loss of ellipticity is usually referred to as Rice's criterion for localization and corresponds to the existence of vanishing eigenvalues of the acoustic tensor. Loss of ellipticity is one criterion amongst others for the detection of instabilities. In particular, it has to be distinguished from loss of strong ellipticity which corresponds to the loss of positive definiteness of the symmetrized acoustic tensor. Classifications of instability criteria can be found in, e.g., (Stein et al., 1995; Nguyen, 2000; Bigoni, 2012; Petryk, 2014) amongst others. In a three-dimensional solid at small strains undergoing tension, loss of ellipticity is usually difficult to achieve unless the model exhibits a sufficiently strong softening behavior, i.e., a strongly negative hardening modulus. In addition, in the case of a smooth yield function, it has been shown by Bigoni and Hueckel (1991) that the critical hardening modulus for strain localization is never positive for associative plasticity at small strains. From a computational point of view, the detection of loss of ellipticity is recast as a minimiza-

tion problem of the determinant of the acoustic tensor over the set of unit normals. Numerical strategies have been proposed in the literature by, e.g., Mosler (2005). More recently, a general and efficient multistart algorithm has been proposed for the detection of loss of ellipticity in elasto-plastic structures by Al Kotob et al. (2019). In multisurface plasticity, also referred to as non-smooth plasticity, the incremental constitutive equations are nonlinear due to the possible activation of multiple mechanisms. In this context, Rice's criterion can be seen as a linearization of the general problem of bifurcation in a band (Petryk, 1992). In addition, this nonlinearity implies that the consequences of loss of ellipticity depend on the stability of the equilibrium. Conditions for shear band bifurcation in multisurface plasticity have been studied by a few authors by exploiting the linearized loss of ellipticity condition (Sawischlewski et al., 1996; Steinmann, 1996) or by addressing the fully nonlinear problem (Petryk, 2000).

Strain localization strongly depends on the plastic yield function. It is reported in the literature that strain localization predictions are highly sensitive to the formation of corners on the current yield surface. The phenomenon of vertex formation has been revealed by calculations based on crystal plasticity and by experimental evidence Cailletaud (1992); Pilvin, 1994. Plasticity theories that take into account singularities on yield surfaces can roughly be divided into two categories, namely, phenomenological models based on the deformation theory of plasticity and non-smooth models based on the classical flow theory of plasticity.

[☆] Fully documented templates are available in the elsarticle package on CTAN.

* Corresponding author.

E-mail address: brian.staber@safrangroup.com (B. Staber).

A first class of phenomenological corner theories has been proposed by Christoffersen and Hutchinson (1979). It is assumed that a corner exists on the yield surface and that it can be represented by a generalized cone in stress space. A general framework is proposed and then specialized to its simplest version known as the J_2 corner theory. The model is built in such a way that it coincides with J_2 deformation theory when stress increments are nearly proportional. This is achieved by taking the instantaneous moduli for nearly proportional loading equal to the tangent moduli of deformation theory. The aforementioned J_2 corner theory has been used by Hutchinson and Tvergaard (1980); Hutchinson and Tvergaard, 1981; Tvergaard et al., 1981; Triantafyllidis et al., 1982; Petryk and Thermann, 1992; Petryk and Thermann, 2002 for instability analysis at large strains and it is observed that a good agreement with experimental data is obtained. According to Hughes and Shakib (1986); Simo, 1987, phenomenological corner theories were not well suited for large-scale simulations because they require one to track corners formation and their evolution. For these reasons, Hughes and Shakib (1986) has proposed a flow theory that mimics corner effects. A smooth yield surface and an associative flow rule are considered but the elasto-plastic moduli decrease as the deviation of the strain rate from proportional loading increases. Similarly, Simo (1987) has proposed a pseudo-corner theory using a smooth yield surface with a non-normality flow rule under the assumption that the plastic strain-rate and strain-rate deviator are coaxial. This model has been used in a few studies such as (Rønning et al., 2010) where classical flow, pseudo-corner and deformation theories are compared in a buckling analysis. Following these ideas, Kuroda and Tvergaard (2001) extended the pseudo-corner model of Simo (1987) by relaxing the coaxial assumption. Furthermore, Kuroda (2015) and Kuroda (2016) incorporated the pseudo-corner model Kuroda and Tvergaard (2001) into strain-gradient plasticity. The common feature of all the aforementioned approaches is a reduction in the instantaneous shear moduli which in turn reduces the predicted bifurcation levels.

The extension of classical flow theory of plasticity to elastic domains formed by independent yield surfaces intersecting non-smoothly has first been carried out by Koiter (1953). The generalization to dependent yield surfaces has been achieved by Mandel (1965) to accommodate crystal plasticity. This formulation of plasticity is commonly referred to as multisurface plasticity and its numerical treatment can be found in Simo et al. (1988). In metal plasticity, the standard threshold such as the Tresca criterion is covered by multisurface plasticity. A fully implicit integration algorithm for the Tresca criterion has been proposed by Perić and de Souza Neto (1999) by having recourse to an optimal parameterization in stress space. The extension of this approach to the Mohr–Coulomb criterion can be found in the textbook de Souza Neto et al. (2011). A generic fully implicit algorithm for multisurface models in principal stress space is presented by Karaoulanis (2013) together with a comprehensive review of methods for handling non-smooth yield surfaces. It should be noted that modern theory of plasticity is based on convex analysis (Moreau, 1976; Suquet, 1981). In this framework, the flow rule of plasticity is written as a differential inclusion involving the subdifferential set of the yield function and the initial boundary value problem is recast into an abstract variational inequality. As a result, non-smooth elastic domains can be considered and multisurface models can be obtained as a special case. Theoretical aspects including mathematical theory and numerical analysis are presented by Han and Reddy (2012) in the context of small perturbations. Although the existence of solutions in finite deformations is still an open problem, recent advances can be found in (Carstensen et al., 2001 and Mielke, 2004) for the incremental boundary value problem. Very recently, a fully implicit subdifferential-based algorithm for the

Mohr–Coulomb criterion has been devised by Sysala et al. (2016). In contrast to multisurface-based algorithms, a single plastic Lagrange multiplier has to be computed and a simpler expression of the consistent tangent matrix can be determined.

The present paper makes the following contributions to the analysis of material instabilities: (a) The influence of non-smooth yield functions on the onset of loss of ellipticity is investigated by considering a family of yield functions that can be written as a linear combination of the principal stresses. Such a family includes classical yield functions such as the Tresca, twin shear stress (Yu, 1983), or the more recent mean influence factor model (Zhang et al., 2020). (b) It is shown that the presence and shape of corners on the yield surface allow for either postponing or advancing loss of ellipticity, or equivalently, decreasing or increasing the critical hardening modulus. (c) Based on the recent work of Al Kotob et al. (2019), a procedure for the numerical detection of loss of ellipticity in multisurface plasticity is proposed. (d) An explicit expression of the subdifferential set for the considered family of yield functions is provided, hence extending existing results in the literature for the Tresca and Mohr–Coulomb criteria (He et al., 2005; Sysala et al., 2017). Such an expression is contained in the abstract form of the flow rule and can be used to, e.g., establish the multisurface form of the flow, or devise an implicit integration algorithm (Sysala et al., 2017). (e) Finite element simulations are performed on simple and realistic geometries in order to illustrate the proposed analysis. It is found that the choice of the yield function has a dramatic effect on the failure of structures. To the authors' best knowledge, such results are not yet reported in the literature.

This paper is organized as follows. First, in Section 2, the theory of plasticity is presented in a convex analysis setting. In Section 3, the conditions for loss of ellipticity in multisurface plasticity are recalled. The family of yield functions considered in this work is described in Section 4 which includes the definition of the flow rule in subdifferential and multisurface forms. The critical hardening moduli and shear bands orientations are then determined for stress states that lie on the smooth portions and corners of the yield surfaces. Finally, in Section 5, numerical illustrations are provided in the case of a cube and a thin plate undergoing tension, and an experimental tubular specimen undergoing tension and torsion.

2. Non-smooth plasticity

In this section, we briefly recall the dual formulation of plasticity under the assumption of small strains. Comprehensive presentations of the theory of plasticity together with computational aspects at finite and small strains can be found in, e.g., (Simo and Hughes, 2006) or (de Souza Neto et al., 2011). Theoretical aspects including mathematical and numerical analysis are presented by Han and Reddy (2012) and the recent review of Reddy (2017).

2.1. Initial boundary value problem and flow rule

Let Ω be a three-dimensional subset of \mathbb{R}^3 with Lipschitz boundary Γ corresponding to the reference configuration occupied by the body of interest \mathcal{B} . The reference configuration undergoes a deformation map $\varphi : \Omega \times \mathcal{T} \rightarrow \mathbb{R}^3$ that results in a deformed configuration Ω_t . Any point in the reference configuration is denoted by $\mathbf{x} \in \Omega$. We denote by $\mathbf{u} : \Omega \times \mathcal{T} \rightarrow \mathbb{R}^3$ the displacement field given by $\mathbf{u}(\mathbf{x}, t) = \varphi(\mathbf{x}, t) - \mathbf{x}$ and let $\boldsymbol{\varepsilon} : \Omega \times \mathcal{T} \rightarrow \mathbb{M}_s^2(\mathbb{R})$ be the second-order infinitesimal strain tensor given by

$$\boldsymbol{\varepsilon}(\mathbf{x}, t) = \frac{1}{2}(\mathbf{u}(\mathbf{x}, t) \otimes \nabla_{\mathbf{x}} + \nabla_{\mathbf{x}} \otimes \mathbf{u}(\mathbf{x}, t)). \quad (1)$$

Based on thermodynamic considerations, the constitutive equations are described in terms of the Helmholtz free energy function ψ . In order to account for plasticity, the strain tensor $\boldsymbol{\varepsilon}$ is additively decomposed into an elastic contribution $\boldsymbol{\varepsilon}^e$ and a plastic contribution $\boldsymbol{\varepsilon}^p$, i.e.,

$$\boldsymbol{\varepsilon}(\mathbf{X}, t) = \boldsymbol{\varepsilon}^e(\mathbf{X}, t) + \boldsymbol{\varepsilon}^p(\mathbf{X}, t). \quad (2)$$

In order to account for hardening, we introduce a symmetric second-order tensor $\boldsymbol{\alpha} : \Omega \times \mathcal{T} \rightarrow \mathbb{M}_S^3(\mathbb{R})$ which models kinematic hardening, and a vector $\mathbf{p} : \Omega \times \mathcal{T} \rightarrow \mathbb{R}^{m_p}$ which models isotropic hardening. Here, $m_p \geq 1$ is an integer that corresponds to the number of internal variables that model isotropic hardening. In most situations, isotropic hardening is described by a single internal variable, i.e., $m_p = 1$. Multiple internal variables can be encountered in the cases of complex isotropic hardening behaviors or multisurface plasticity. For instance, in the case of single crystal plasticity, m_p can be equal to the number of crystal systems. Let then \mathbf{X} and \mathbf{R} be the symmetric second-order tensor and the vector which are conjugate to $\boldsymbol{\alpha}$ and \mathbf{p} , respectively. The Helmholtz free energy function, assumed to be a function of the elastic strain tensor $\boldsymbol{\varepsilon}^e := \boldsymbol{\varepsilon} - \boldsymbol{\varepsilon}^p$ and of the hardening variables $\boldsymbol{\alpha}$ and \mathbf{p} , is further decomposed as

$$\psi(\boldsymbol{\varepsilon}^e, \boldsymbol{\alpha}, \mathbf{p}) = \psi_e(\boldsymbol{\varepsilon}^e) + \psi_p(\boldsymbol{\alpha}, \mathbf{p}), \quad (3)$$

where ψ_e and ψ_p denote the elastic and inelastic contributions, respectively. In the context of linearized plasticity, the elastic free energy function is chosen as $\psi_e(\boldsymbol{\varepsilon}^e) = (1/2)\boldsymbol{\varepsilon}^e : \mathbb{C} : \boldsymbol{\varepsilon}^e$ where \mathbb{C} denotes the fourth-order elasticity tensor. Following the Clausius–Duhem inequality, the Cauchy stress tensor $\boldsymbol{\sigma}$ and the conjugate forces \mathbf{X} and \mathbf{R} are given by

$$\boldsymbol{\sigma} = \mathbb{C} : \boldsymbol{\varepsilon}^e, \quad \mathbf{X} = -\frac{\partial \psi_p}{\partial \boldsymbol{\alpha}}, \quad \mathbf{R} = -\frac{\partial \psi_p}{\partial \mathbf{p}}. \quad (4)$$

The second-order tensor \mathbf{X} corresponds to the back-stress and the entries of the vector $\mathbf{R} = (R_1, \dots, R_{m_p})$ correspond to yield stresses that define the yield surface. In what follows, \mathcal{S} and \mathcal{P} denote the sets of generalized stresses and rate plastic variables such that $(\boldsymbol{\sigma}, \mathbf{X}, \mathbf{R}) \in \mathcal{S}$ and $(\dot{\boldsymbol{\varepsilon}}^p, \dot{\boldsymbol{\alpha}}, \dot{\mathbf{p}}) \in \mathcal{P}$. Arbitrary triplets in \mathcal{P} and \mathcal{S} will be denoted by $(\mathbf{A}, \mathbf{B}, \mathbf{c})$ and $(\tilde{\boldsymbol{\sigma}}, \tilde{\mathbf{X}}, \tilde{\mathbf{R}})$, respectively. The evolution of the plastic strain tensor and hardening variables is described in terms of an elastic domain \mathbb{E} . Let then $N_{\mathbb{E}}(\boldsymbol{\sigma}, \mathbf{X}, \mathbf{R})$ be the normal cone to the elastic region \mathbb{E} at $(\boldsymbol{\sigma}, \mathbf{X}, \mathbf{R}) \in \mathcal{S}$,

$$N_{\mathbb{E}}(\boldsymbol{\sigma}, \mathbf{X}, \mathbf{R}) = \left\{ (\mathbf{A}, \mathbf{B}, \mathbf{c}) \in \mathcal{P} \mid \mathbf{A} : (\boldsymbol{\sigma} - \tilde{\boldsymbol{\sigma}}) + \mathbf{B} : (\mathbf{X} - \tilde{\mathbf{X}}) + \mathbf{c} \cdot (\mathbf{R} - \tilde{\mathbf{R}}) \geq 0, \forall (\tilde{\boldsymbol{\sigma}}, \tilde{\mathbf{X}}, \tilde{\mathbf{R}}) \in \mathbb{E}_j \right\}, \quad (5)$$

and let $\partial\phi$ be the multi-valued subdifferential set of the yield function, i.e.,

$$\partial\phi(\boldsymbol{\sigma}, \mathbf{X}, \mathbf{R}) = \left\{ (\mathbf{A}, \mathbf{B}, \mathbf{c}) \in \mathcal{P} \mid \phi(\tilde{\boldsymbol{\sigma}}, \tilde{\mathbf{X}}, \tilde{\mathbf{R}}) \geq \phi(\boldsymbol{\sigma}, \mathbf{X}, \mathbf{R}) + \mathbf{A} : (\tilde{\boldsymbol{\sigma}} - \boldsymbol{\sigma}) + \mathbf{B} : (\tilde{\mathbf{X}} - \mathbf{X}) + \mathbf{c} \cdot (\tilde{\mathbf{R}} - \mathbf{R}), \forall (\tilde{\boldsymbol{\sigma}}, \tilde{\mathbf{X}}, \tilde{\mathbf{R}}) \in \mathcal{S} \right\}. \quad (6)$$

The evolution of the plastic and internal variables are governed by the abstract flow rule

$$(\dot{\boldsymbol{\varepsilon}}^p, \dot{\boldsymbol{\alpha}}, \dot{\mathbf{p}}) \in N_{\mathbb{E}}(\boldsymbol{\sigma}, \mathbf{X}, \mathbf{R}), \quad (7)$$

which can be seen as an alternative formulation of the principle of maximum dissipation. The elastic domain is expressed in terms of a yield function ϕ as follows

$$\mathbb{E} = \left\{ (\tilde{\boldsymbol{\sigma}}, \tilde{\mathbf{X}}, \tilde{\mathbf{R}}) \in \mathcal{S} \mid \phi(\tilde{\boldsymbol{\sigma}}, \tilde{\mathbf{X}}, \tilde{\mathbf{R}}) \leq 0 \right\}, \quad (8)$$

where it is assumed that \mathbb{E} is a closed convex set that contains the origin, i.e., $\phi(\mathbf{0}, \mathbf{0}, \mathbf{0}) \leq 0$. Based on results in convex analysis (Han and Reddy, 2012; Reddy, 2017), the abstract flow rule given by Eq. (7) can also be written in terms of the subdifferential set $\partial\phi$,

$$(\dot{\boldsymbol{\varepsilon}}^p, \dot{\boldsymbol{\alpha}}, \dot{\mathbf{p}}) \in \dot{\gamma} \partial\phi(\boldsymbol{\sigma}, \mathbf{X}, \mathbf{R}), \quad (9)$$

where $\dot{\gamma}$ is a Lagrange multiplier that satisfies the Karush–Kuhn–Tucker conditions (Eve et al., 1990; Eve et al., 1990)

$$\dot{\gamma} \geq 0, \quad \phi(\boldsymbol{\sigma}, \mathbf{X}, \mathbf{R}) \leq 0, \quad \dot{\gamma} \phi(\boldsymbol{\sigma}, \mathbf{X}, \mathbf{R}) = 0.$$

A yield function linear with respect to the principal stresses will be chosen in Section 4 and an explicit expression of its subdifferential set is provided in A. We end this section by recalling the boundary value problem of interest. Essential and natural boundary conditions are applied on the partitions Γ_D and Γ_N of Γ , with $\Gamma_D \cap \Gamma_N = \emptyset$ and $\Gamma = \Gamma_D \cup \Gamma_N$. Under the assumption of a quasi-static deformation process, the strong formulation of the initial boundary value problem takes the form

$$-\mathbf{V} \cdot \boldsymbol{\sigma} = \mathbf{f}, \quad \text{in } \Omega_t \times \mathcal{T}, \quad (10a)$$

$$\boldsymbol{\sigma} \mathbf{n} = \mathbf{t}_d, \quad \text{on } \Gamma_N \times \mathcal{T}, \quad (10b)$$

$$\mathbf{u} = \mathbf{u}_d, \quad \text{on } \Gamma_D \times \mathcal{T}, \quad (10c)$$

where $\boldsymbol{\sigma} : \Omega \times \mathcal{T} \rightarrow \mathbb{M}_S^3(\mathbb{R})$ is the second-order Cauchy stress tensor, $\mathbf{f} \in \mathbb{R}^3$ describes the volume forces, and \mathbf{n} is the outward unit normal at $\mathbf{x} \in \Gamma_N$.

2.2. Multisurface plasticity deduced from convex analysis

In the sequel of this work, the analysis of material instabilities is performed by relying on the multisurface form of the flow rule. Hence, this section briefly describes how the multisurface flow rule can be deduced from the abstract flow rule (7). We consider elastic regions \mathbb{E} formed by subsets $\mathbb{E}_j \subset \mathcal{S}$ that intersect non-smoothly, where \mathcal{S} denotes the set of generalized stresses. Hence, the elastic domain is assumed to take the form $\mathbb{E} = \bigcap_{j=1}^m \mathbb{E}_j$ with

$$\mathbb{E}_j = \left\{ (\tilde{\boldsymbol{\sigma}}, \tilde{\mathbf{X}}, \tilde{\mathbf{R}}_j) \in \mathcal{S} \mid \phi_j(\tilde{\boldsymbol{\sigma}}, \tilde{\mathbf{X}}, \tilde{\mathbf{R}}_j) \leq 0 \right\}, \quad j = 1, \dots, m, \quad (11)$$

where ϕ_j is j -th yield function associated to the elastic domain \mathbb{E}_j . If there exists a family $\{\mu_j\}_{j=1}^m$ of positive real scalars such that

$$\phi(\boldsymbol{\sigma}, \mathbf{X}, \mathbf{R}) = \sum_{j=1}^m \mu_j \phi_j(\boldsymbol{\sigma}, \mathbf{X}, R_j), \quad (12)$$

then it has been shown by Clarke (1990) that $\partial\phi$ takes the form

$$\partial\phi(\boldsymbol{\sigma}, \mathbf{X}, \mathbf{R}) = \left\{ \mathbf{M} \in \mathbb{M}_S^3 \mid \mathbf{M} = \sum_{j=1}^m \mu_j \mathbf{M}_j, \mathbf{M}_j \in \partial\phi_j(\boldsymbol{\sigma}, \mathbf{X}, R_j) \right\}, \quad (13)$$

where $\partial\phi_j$ is the subdifferential set associated to ϕ_j . Assuming that the yield functions $\phi_j, j = 1, \dots, m$, are smooth functions of the generalized stresses, the subdifferential sets $\partial\phi_j$ are simply given by the singletons

$$\partial\phi_j = \left\{ (\dot{\boldsymbol{\varepsilon}}^p, \dot{\boldsymbol{\alpha}}, \dot{\mathbf{p}}_j) = \left(\nabla_{\boldsymbol{\sigma}} \phi_j, \nabla_{\mathbf{X}} \phi_j, \nabla_{R_j} \phi_j \right) \right\}, \quad j = 1, \dots, m, \quad (14)$$

and the abstract flow rule given by Eq. (9) reduces to

$$\dot{\boldsymbol{\varepsilon}}^p = \sum_{j=1}^m \dot{\gamma}_j \nabla_{\boldsymbol{\sigma}} \phi_j, \quad \dot{\boldsymbol{\alpha}} = -\sum_{j=1}^m \dot{\gamma}_j \nabla_{\mathbf{X}} \phi_j, \quad \dot{\mathbf{p}} = -\sum_{j=1}^m \dot{\gamma}_j \nabla_{R_j} \phi_j, \quad (15)$$

which corresponds to Koiter's form of the flow rule. The Lagrange multipliers $\dot{\gamma}_1, \dots, \dot{\gamma}_m$ are solutions to the problem

$$\dot{\gamma}_j \geq 0, \quad \phi_j(\boldsymbol{\sigma}, \mathbf{X}, R_j) \leq 0, \quad \dot{\gamma}_j \phi_j(\boldsymbol{\sigma}, \mathbf{X}, R_j) = 0, \quad \dot{\gamma}_j \dot{\phi}_j = 0, \quad j = 1, \dots, m, \quad (16)$$

which corresponds to the set of Karush–Kuhn–Tucker and consistency conditions. The Lagrange multipliers $\dot{\gamma}_1, \dots, \dot{\gamma}_m$ are related to

$\dot{\gamma}$ and μ_1, \dots, μ_m through the relationships (Koiter, 1953; Mandel, 1965)

$$\dot{\gamma}_j = \dot{\gamma} \mu_j, \quad j = 1, \dots, m.$$

Eq. (15) complemented by the conditions (16) is referred to as a multisurface model for continuously differentiable yield functions that intersect non-smoothly. Let \mathbb{J} be the set defined as $\mathbb{J} = \{J \in \{1, \dots, m\} : f_J = 0\}$ and let by $M_{act} = \text{Card}(\mathbb{J})$ be the number of active mechanisms. Using the constitutive Eqs. (4) together with the chosen form of the canonical yield function, one has the following rate constitutive equations (Koiter, 1953; Mandel, 1965)

$$\begin{aligned} \dot{\boldsymbol{\sigma}}(\dot{\boldsymbol{\varepsilon}}) &= \mathbb{C} : \dot{\boldsymbol{\varepsilon}} - \sum_{J \in \mathbb{J}} \mathbb{C} : \mathbf{N}_J \dot{\gamma}_J, \quad \dot{\mathbf{X}} = \sum_{J \in \mathbb{J}} \mathbb{K}(\boldsymbol{\alpha}) : \mathbf{N}_J \dot{\gamma}_J, \quad \dot{R}_I \\ &= \sum_{J \in \mathbb{J}} H_{IJ}(\mathbf{p}) \dot{\gamma}_J, \end{aligned} \quad (17)$$

where $\mathbf{N}_I = \nabla_{\boldsymbol{\sigma}} \phi_I$ is the normal tensor to the I -th yield surface, $\mathbb{K} = \nabla_{\boldsymbol{\alpha}}^2 \psi_p$ and $[H] = \nabla_{\mathbf{p}}^2 \psi_p$ are the kinematic and isotropic hardening moduli, respectively. For a given strain rate, the non-negative Lagrange multipliers $\{\dot{\gamma}_J\}_{J \in \mathbb{J}}$ can be obtained by invoking the consistency conditions $\dot{\gamma}_J \dot{\phi}_J = 0$ for $J \in \mathbb{J}$. By successively applying the chain rule, one finds the classical rate equation

$$\begin{aligned} \dot{\phi}_J(\boldsymbol{\sigma}, \mathbf{X}, \mathbf{R}) &= \nabla_{\boldsymbol{\sigma}} \phi_J(\boldsymbol{\sigma}, \mathbf{X}, \mathbf{R}) : \dot{\boldsymbol{\sigma}} + \nabla_{\mathbf{X}} \phi_J(\boldsymbol{\sigma}, \mathbf{X}, \mathbf{R}) \\ &: \dot{\mathbf{X}} + \nabla_{\mathbf{R}} \phi_J(\boldsymbol{\sigma}, \mathbf{X}, \mathbf{R}) \dot{R}_J, \end{aligned} \quad (18)$$

which together with Eq. (17), leads to the following non-linear system of equations for the non-negative Lagrange multipliers (Petryk, 2000):

$$\sum_{J \in \mathbb{J}} G_{IJ}(\boldsymbol{\alpha}, \mathbf{p}) \dot{\gamma}_J = \mathbf{N}_I : \mathbb{C} : \dot{\boldsymbol{\varepsilon}}, \quad I \in \mathbb{J}, \quad (19)$$

where the coefficients G_{IJ} are given by

$$G_{IJ}(\boldsymbol{\alpha}, \mathbf{p}) = \chi_{IJ} + \varsigma_{IJ}(\boldsymbol{\alpha}) + H_{IJ}(\mathbf{p}), \quad 1 \leq I, J \leq m, \quad (20)$$

with $\chi_{IJ} \equiv \mathbf{N}_I : \mathbb{C} : \mathbf{N}_J$ and $\varsigma_{IJ}(\boldsymbol{\alpha}) = \mathbf{N}_I : \mathbb{K}(\boldsymbol{\alpha}) : \mathbf{N}_J$. The existence of solutions to the problem defined by Eq. (19) is discussed in (Petryk, 2000). By plugging the solution to Eq. (20) into Eq. (17), it is found that the elasto-plastic tangent tensor \mathbb{C}^{ep} , defined such that

$$\dot{\boldsymbol{\sigma}}(\dot{\boldsymbol{\varepsilon}}) = \mathbb{C}^{ep}(\dot{\boldsymbol{\varepsilon}}) : \dot{\boldsymbol{\varepsilon}}, \quad (21)$$

is given by (Koiter, 1953; Mandel, 1965)

$$\mathbb{C}^{ep}(\dot{\boldsymbol{\varepsilon}}) = \mathbb{C} - \sum_{J \in \mathbb{J}} \mathbb{C} : \mathbf{N}_J \otimes \tilde{\mathbf{N}}_J : \mathbb{C}, \quad \tilde{\mathbf{N}}_J = \sum_{K \in \mathbb{J}} \tilde{G}_{JK}^{-1}(\boldsymbol{\alpha}, \mathbf{p}) \mathbf{N}_K, \quad (22)$$

where $\tilde{G}_{JK}^{-1}(\boldsymbol{\alpha}, \mathbf{p})$ denote the entries of the inverse matrix of the matrix $\left[\tilde{G}(\boldsymbol{\alpha}, \mathbf{p}) \right]$ which gathers the coefficients $G_{MN}(\boldsymbol{\alpha}, \mathbf{p})$ for $(M, N) \in \mathbb{J} \times \mathbb{J}$. It should be noted that the incremental constitutive Eq. (21) is nonlinear due to its dependence on the set of active mechanisms \mathbb{J} . Such a nonlinearity does not appear in smooth plasticity and plays an important role in the prediction of material instabilities as shown by Petryk (1992). Other examples of incrementally nonlinear models can be found, for instance, in the work of Chambon et al. (2000) in the case of geomaterials.

3. Conditions for shear band bifurcation in non-smooth plasticity

This section is concerned with material instabilities due to the development of first-order weak discontinuities. Following Rice (1976), let $\nabla \dot{\mathbf{u}}^{(0)}$ be a homogeneous solution to the rate boundary value problem. We are concerned with solutions involving the

existence of a shear band, i.e., the strain-rate is given by $\nabla \dot{\mathbf{u}}^{(0)}$ outside the shear band and given by

$$\nabla \dot{\mathbf{u}}^{(1)} = \nabla \dot{\mathbf{u}}^{(0)} + \mathbf{g} \otimes \mathbf{n} \quad (23)$$

inside the shear band, where $\mathbf{n} \in \mathcal{S}$ denotes the normal to the shear band and \mathbf{g} is an arbitrary vector to be determined. Furthermore, the rate traction vector is assumed to be continuous across the band, i.e.,

$$(\dot{\boldsymbol{\sigma}}^{(1)} - \dot{\boldsymbol{\sigma}}^{(2)}) \cdot \mathbf{n} = \mathbf{0}. \quad (24)$$

By introducing the jumps $[[\nabla \dot{\mathbf{u}}]] \equiv \nabla \dot{\mathbf{u}}^{(1)} - \nabla \dot{\mathbf{u}}^{(0)}$ and $[[\dot{\boldsymbol{\sigma}} \cdot \mathbf{n}]] = \mathbf{0}$, the above kinematical and statical conditions are often summarized as (Rice, 1976)

$$[[\nabla \dot{\mathbf{u}}]] = \mathbf{g} \otimes \mathbf{n}, \quad [[\dot{\boldsymbol{\sigma}}]] \cdot \mathbf{n} = \mathbf{0}. \quad (25)$$

In the case of an incrementally linear operator \mathbb{L}^{ep} such that $\dot{\boldsymbol{\sigma}}(\dot{\boldsymbol{\varepsilon}}) = \mathbb{L}^{ep} : \dot{\boldsymbol{\varepsilon}}$, the conditions (25) lead the well-known loss of ellipticity condition

$$\mathbb{L}^{ep} \circ (\mathbf{n} \otimes \mathbf{n}) \cdot \mathbf{g} = \mathbf{0}, \quad (26)$$

where $(\mathbb{L} \circ \mathbf{n} \otimes \mathbf{n})_{ik} = \mathbb{L}_{ijkl} n_j n_l$. The condition (26) is also commonly referred to as Rice's criterion for strain localization. While it provides a sufficient condition in smooth plasticity with two branches, in the case of an incrementally nonlinear model as (21), such a loss of ellipticity condition is obtained by linearizing the condition (25) as pointed out by Petryk (1992). By carrying out the linearization of (25) near the uniform strain-rate $\dot{\boldsymbol{\varepsilon}}^{(0)}$, one has

$$\mathbf{Q}_{ep}^{(0)}(\mathbf{n}) \cdot \mathbf{g} = \mathbf{0}, \quad \mathbf{Q}_{ep}^{(0)}(\mathbf{n}) \equiv \mathbb{C}^{ep}(\dot{\boldsymbol{\varepsilon}}^{(0)}) \circ \mathbf{n} \otimes \mathbf{n}. \quad (27)$$

Conditions for bifurcation in a band in the case of incrementally nonlinear operators have been proposed by Petryk (1992). A sufficient condition for a shear band with orientation \mathbf{n} to take place in a infinite body deforming with $\nabla \dot{\mathbf{u}}^{(0)}$ is given by: There exists $\mathbf{n}^* \in \mathcal{S}$ such that

$$\det(\mathbf{Q}_{ep}^{(0)}(\mathbf{n}^*)) \leq 0, \quad (28)$$

provided that

$$\begin{aligned} U(\mathbf{g} \otimes \mathbf{n}^*) &\equiv \frac{1}{2} (\mathbf{g} \otimes \mathbf{n}^*) : \mathbb{C}^{ep}((\mathbf{g} \otimes \mathbf{n}^*)_s) : (\mathbf{g} \otimes \mathbf{n}^*) \\ &> 0, \quad \forall \mathbf{g} \neq \mathbf{0}. \end{aligned} \quad (29)$$

Condition (29) represents a local condition for stability of equilibrium where the incremental operator is evaluated at the strain-rate $(\mathbf{g} \otimes \mathbf{n}^*)_s = (1/2)(\mathbf{g} \otimes \mathbf{n}^* + \mathbf{n}^* \otimes \mathbf{g})$. In this work, we restrict our analytical and numerical analyses to the loss of ellipticity condition (28). The consideration of the condition (29) will be explored in future works. In the subsequent sections, \mathbf{Q}_{el} denotes the elastic acoustic tensor given by $\mathbf{Q}_{el}(\mathbf{n}) = \mathbb{C} \circ (\mathbf{n} \otimes \mathbf{n})$. Furthermore, the following assumptions are made:

(H1) The material under consideration is isotropic. In this case, the elastic acoustic tensor is given by $\mathbf{Q}_{el}(\mathbf{n}) = (\lambda + 2\mu)\mathbf{n} \otimes \mathbf{n} + \mu([1] - \mathbf{n} \otimes \mathbf{n})$ and its inverse takes the form

$$\mathbf{Q}_{el}^{-1}(\mathbf{n}) = -\frac{(\lambda + \mu)}{\mu(\lambda + 2\mu)} \mathbf{n} \otimes \mathbf{n} + \frac{1}{\mu} [1]. \quad (30)$$

It can also be shown that $\det(\mathbf{Q}_{el}(\mathbf{n})) \neq 0$ for any normal vector \mathbf{n} .

(H2) The hardening matrix $[H]$ is symmetric. As a result, the acoustic tensor \mathbf{Q}_{ep} and tangent tensor \mathbb{C}^{ep} are both symmetric. The interested reader is referred to Petryk (1992) regarding the consequences of these symmetry properties.

(H3) The number of active mechanisms M_{act} is such that $M_{\text{act}} = 2$. The consequences of this restriction will be highlighted in Section 3.2.

The case of a single active mechanism, well reported in the literature (Bigoni and Hueckel, 1991; Besson et al., 2009), is first recalled in Section 3.1. The case of multiple active mechanisms, previously studied by Sawischlewski et al. (1996) and Petryk (2000), is described in Section 3.2. Finally, a numerical procedure is described in Section 3.3 by relying on the recent algorithm proposed by Al Kotob et al. (2019).

3.1. Case of a single active mechanism

We first assume that the current stress state lies on a smooth portion of the yield surface, i.e., $\varphi_K = 0$ for some $K \in \{1, \dots, m\}$. In this case, the tangent elasto-plastic tensor given by Eq. (22) reduces to

$$\mathbb{C}^{\text{ep}} = \mathbb{C} - \frac{(\mathbb{C} : \mathbf{N}_K) \otimes (\mathbf{N}_K : \mathbb{C})}{\chi_{KK} + H_{KK}}, \quad \chi_{KK} = \mathbf{N}_K : \mathbb{C} : \mathbf{N}_K. \quad (31)$$

By injecting the above expression into the acoustic tensor \mathbf{Q}_{ep} and assuming that the hardening modulus decreases with the plastic strain, the highest hardening modulus fulfilling the condition $\det(\mathbf{Q}_{\text{ep}}^{(0)}(\mathbf{n})) = 0$, referred to as the critical hardening modulus, is given by Bigoni and Hueckel (1991) and Besson et al. (2009)

$$H_K^{\text{crit}}(\mathbf{n}) = \max_{\mathbf{n}, \|\mathbf{n}\|=1} \langle \mathbf{d}(\mathbf{n}), \mathbf{Q}_{\text{el}}^{-1}(\mathbf{n}) \mathbf{d}(\mathbf{n}) \rangle - \mathbf{N}_K : \mathbb{C} : \mathbf{N}_K, \quad (32)$$

with $\mathbf{d}(\mathbf{n}) = (\mathbb{C} : \mathbf{N}_K) \mathbf{n}$. Let then $\{N_j^K\}_{j=1}^3$ be the set of entries of \mathbf{N}_K on the principal basis. The optimization problem given by Eq. (32) is equivalent to the maximization of a Lagrangian function, leading to

$$n_j \left((N_j^K)^2 - \frac{1}{1-\nu} \sum_{i=1}^3 (n_i^2 N_i^K) N_j^K - \frac{\beta}{4\mu} \right) = 0, \quad j \in \{1, 2, 3\}, \quad (33)$$

where β is a Lagrange multiplier associated to the normalisation constraint $\|\mathbf{n}\|^2 = 1$. Different cases have to be distinguished depending on the values of n_1, n_2 , and n_3 and the following solutions can be found (see Bigoni and Hueckel (1991)). If n_1, n_2 , and n_3 are non-zero, then the system is indeterminate and there are no solutions. If $n_i \neq 0, n_j \neq 0, n_k = 0$, and $n_i \neq n_j$, then

$$H_K^{\text{crit}}(\mathbf{n}) = -E (N_k^K)^2, \quad n_i^2 = \frac{N_i^K + \nu N_k^K}{N_i^K - N_j^K}, \quad n_j^2 = 1 - n_i^2. \quad (34)$$

In this case, the eigenvector \mathbf{g} in Eq. (26) can be decomposed onto the principal basis as $\mathbf{g} = \sum_{i=1}^3 g_i \mathbf{m}_i \otimes \mathbf{m}_i$ where the components g_1, g_2, g_3 are given by

$$g_i = (N_i^K - N_j^K) n_i, \quad g_j = (N_j^K - N_i^K) n_j, \quad g_k = 0. \quad (35)$$

Finally, if $n_i = 1$ and $n_j = n_k = 0$, then

$$H_K^{\text{crit}}(\mathbf{n}) = -2\mu \left(\frac{(N_j^K + \nu N_k^K)^2}{1-\nu} + (1+\nu) (N_k^K)^2 \right). \quad (36)$$

As a result, the critical hardening modulus for strain localization is never strictly positive whenever a single mechanism is active.

3.2. Case of multiple active mechanisms

We now consider the case where the current stress state lies on a corner of the yield surface, resulting in multiple active mechanisms. Using the general expression of \mathbb{C}^{ep} given by Eq. (22) for multisurface plasticity, the acoustic tensor $\mathbf{Q}_{\text{ep}}^{(0)}$ takes the form

$$\mathbf{Q}_{\text{ep}}^{(0)}(\mathbf{n}) = \mathbf{Q}_{\text{el}}(\mathbf{n}) - \sum_{J \in \mathbb{J}} ((\mathbb{C} : \mathbf{N}_J) \mathbf{n}) \otimes ((\tilde{\mathbf{N}}_J : \mathbb{C}) \mathbf{n}), \quad (37)$$

where $\tilde{\mathbf{N}}_J$ is defined in Eq. (22). It is worth pointing out that the above acoustic tensor depends on the strain-rate $\dot{\epsilon}^{(0)}$ implicitly through the set of active mechanisms \mathbb{J} . Let $\bar{\mathbf{Q}}_{\text{ep}}^{(0)}(\mathbf{n})$ be the normalized acoustic tensor defined such that $\mathbf{Q}_{\text{ep}}^{(0)}(\mathbf{n}) = \mathbf{Q}_{\text{el}}(\mathbf{n}) \bar{\mathbf{Q}}_{\text{ep}}^{(0)}(\mathbf{n})$, that is

$$\bar{\mathbf{Q}}_{\text{ep}}^{(0)}(\mathbf{n}) = [\mathbf{1}] - \sum_{J \in \mathbb{J}} \mathbf{Q}_{\text{el}}^{-1}(\mathbf{n}) ((\mathbb{C} : \mathbf{N}_J) \mathbf{n}) \otimes ((\tilde{\mathbf{N}}_J : \mathbb{C}) \mathbf{n}). \quad (38)$$

The determinant of $\mathbf{Q}_{\text{ep}}^{(0)}$ can be written as $\det(\mathbf{Q}_{\text{ep}}^{(0)}(\mathbf{n})) = \det(\mathbf{Q}_{\text{el}}(\mathbf{n})) \det(\bar{\mathbf{Q}}_{\text{ep}}^{(0)}(\mathbf{n}))$. Let $[\pi(\mathbf{n})]$ be the $M_{\text{act}} \times M_{\text{act}}$ matrix defined component-wise as

$$\pi_{IJ}(\mathbf{n}) \equiv \langle (\mathbf{N}_K : \mathbb{C}) \mathbf{n}, \mathbf{Q}_{\text{el}}^{-1}(\mathbf{n}) (\mathbf{N}_L : \mathbb{C}) \mathbf{n} \rangle, \quad 1 \leq I, J \leq M_{\text{act}}, \quad (K, L) \in \mathbb{J} \times \mathbb{J}, \quad (39)$$

where it is recalled that $M_{\text{act}} = \text{Card}(\mathbb{J})$ denotes the number of active yield surfaces. Using the expression of $\mathbf{Q}_{\text{el}}^{-1}(\mathbf{n})$, the matrix $[\pi(\mathbf{n})]$ defined by Eq. (39) can be rewritten as

$$\pi_{IJ}(\mathbf{n}) = -\frac{4\mu(\lambda + \mu)}{\lambda + 2\mu} \langle \mathbf{n}, \mathbf{N}_K \mathbf{n} \rangle \langle \mathbf{n}, \mathbf{N}_L \mathbf{n} \rangle + 4\mu \langle \mathbf{N}_K \mathbf{n}, \mathbf{N}_L \mathbf{n} \rangle. \quad (40)$$

By analyzing the eigenvalue problem for the update matrix in Eq. (38), it can be deduced that

$$\det(\bar{\mathbf{Q}}_{\text{ep}}^{(0)}(\mathbf{n})) = \det\left([\tilde{\mathbf{G}}]^{-1}\right) \det\left([\tilde{\mathbf{G}}] - [\pi(\mathbf{n})]\right), \quad (41)$$

where it is recalled that $[\tilde{\mathbf{G}}]$ gathers the entries G_{MN} for $(M, N) \in \mathbb{J} \times \mathbb{J}$ (see Eq. 22). Petryk (2000) shows that there exist lower and upper bounds, t_l and t_u , for the time t^* at which a primary bifurcation in a band takes place. Given our restriction to the case of at most two active mechanisms, $M_{\text{act}} = 2$, provided that $H_{11} > H_k^{\text{crit}}$ and $H_{22} > H_k^{\text{crit}}$ with H_k^{crit} being the critical hardening modulus in the case of a single active mechanism, the lower and upper bounds coincide and the theoretical results of Petryk (2000) simplify to the single condition: Find $\mathbf{n} \in \mathcal{S}$ such that

$$\det([\pi(\mathbf{n})] - [\tilde{\mathbf{G}}]) = 0, \quad \tilde{\mathbf{G}}_{IJ} = \mathbf{N}_J : \mathbb{C} : \mathbf{N}_J + H_{IJ}, \quad (I, J) \in \mathbb{J} \times \mathbb{J}. \quad (42)$$

This loss of ellipticity condition has also been obtained by Sawischlewski et al. (1996) and Steinmann (1996) for small and large strains, respectively, by relying on the linearized condition of loss of ellipticity. However, for $M_{\text{act}} > 2$, (42) is generally not necessary for bifurcation in a band according to Petryk (2000). In summary, in the case considered herein, the detection of material instabilities consists in two steps:

- Solving the problem given by Eq. (42) that yields a normal vector \mathbf{n}^* if a solution exists. The associated eigenvector \mathbf{g}^* that spans the null space of the acoustic tensor can then be determined.
- Checking if the local condition of equilibrium stability (29) holds for \mathbf{n}^* .

In this study, the analytical and numerical analyses are restricted to the loss of ellipticity condition (42) while the analysis of the local stability condition (29) has been left for future works. In the case of two active mechanisms, Sawischlewski et al. (1996) provide explicit expressions of the critical hardening modulus. Recall that the matrix \tilde{G} is given by $\tilde{G} = \tilde{\chi} + \tilde{H}$. If $[\pi(\mathbf{n})] - \tilde{\chi}$ is invertible, Eq. (42) reduces to

$$\det([\pi(\mathbf{n})] - \tilde{\chi} - \tilde{H}) = \det([\pi(\mathbf{n})] - \tilde{\chi}) + \det([\tilde{H}]) + \text{adj}([\pi(\mathbf{n})] - \tilde{\chi}) : [\tilde{H}]. \quad (43)$$

In this case, explicit expressions of the critical hardening moduli are given by Sawischlewski et al. (1996) for a family of matrices $[\tilde{H}(\ell)]$ given by

$$[\tilde{H}(\ell)] \equiv H_\ell(\ell i_m) + (1 - \ell)[1], \quad (44)$$

where H_ℓ is a scalar hardening modulus and $i_m = 1$ for all $I, J \in \{1, \dots, M_{\text{act}}\}^2$. For brevity, only the particular case $\ell = 1$ that will be considered in the sequel of this work is recalled. For $\ell = 1$, it is found that $\det([\tilde{H}(\ell)]) = 0$ and that Eq. (43) reduces to

$$\det([\pi(\mathbf{n})] - \tilde{\chi}) - \text{Hadj}([\pi(\mathbf{n})] - \tilde{\chi}) : i_m = 0. \quad (45)$$

Hence, it can be deduced that the critical scalar hardening modulus H^{crit} is given by

$$H^{\text{crit}} = \max_{|i_m|=1} \left(([\pi(\mathbf{n})] - \tilde{\chi})^{-1} : i_m \right). \quad (46)$$

The cases $\ell = 0$ and $\ell \neq 1$ are reported in C. It should be emphasized that the analysis presented in this section is valid under the constraint that the matrix $[\tilde{G}(\ell)]$ given by $[\tilde{G}(\ell)] = \tilde{\chi} + [\tilde{H}(\ell)]$ is nonsingular. For $\ell = 1$, the matrix $[G(\ell)]$ is singular for the hardening modulus

$$H_\ell = -3\mu, \quad (47)$$

which is strongly negative.

3.3. Numerical detection of loss of ellipticity in non-smooth plasticity

In this section, the recent algorithm proposed by Al Kotob et al. (2019) for the detection of loss of ellipticity is specified for multi-surface plasticity. The algorithm draws on the approach proposed by Mosler (2005) together with an efficient multistart strategy. The optimization problem raised by the condition of the onset of loss of ellipticity is recast into the minimization problem: Find \mathbf{n}^* such that

$$\det([\pi(\mathbf{n}^*)] - [\tilde{G}]) = \min_{\mathbf{n} \in \mathcal{S}} \det([\pi(\mathbf{n})] - [\tilde{G}]). \quad (48)$$

Let then $\mathbf{r} : \mathcal{S} \rightarrow \mathbb{R}^3$ be the residual vector defined as

$$\mathbf{r}(\mathbf{n}) = \frac{\partial}{\partial \mathbf{n}} \det([\pi(\mathbf{n})] - [\tilde{G}]). \quad (49)$$

For notational convenience, we let $[\tilde{\pi}(\cdot)] = [\pi(\cdot)] - [\tilde{G}]$. The following identities will be useful for the developments of this section:

$$\frac{\partial \det([\tilde{\pi}])}{\partial [\tilde{\pi}]} = \det([\tilde{\pi}])([\tilde{\pi}]^{-1})^T, \quad \frac{\partial [\tilde{\pi}]^{-1}}{\partial [\tilde{\pi}]} = -[\tilde{\pi}]^{-1} \boxtimes [\tilde{\pi}]^{-1}, \quad (50)$$

and the adjugate matrix $\det([\tilde{\pi}])[\tilde{\pi}]^{-1}$ will be denoted as $\text{adj}([\tilde{\pi}])$. It can then be deduced that the residual \mathbf{r} vector takes the form

$$\mathbf{r}(\mathbf{n}) = [\text{adj}([\tilde{\pi}(\mathbf{n})])] : \frac{\partial [\pi(\mathbf{n})]}{\partial \mathbf{n}}, \quad (51)$$

where the first-order partial derivatives of $[\pi(\mathbf{n})]$ with respect to \mathbf{n} are given by

$$\frac{\partial \pi_{IJ}(\mathbf{n})}{\partial \mathbf{n}} = \alpha_1 \langle \mathbf{n}, \mathbf{N}_I \mathbf{n} \rangle (\mathbf{N}_J \mathbf{n} + \mathbf{N}_J^T \mathbf{n}) + \alpha_1 \langle \mathbf{n}, \mathbf{N}_J \mathbf{n} \rangle (\mathbf{N}_I \mathbf{n} + \mathbf{N}_I^T \mathbf{n}) + \alpha_2 (\mathbf{N}_I^T \mathbf{N}_J \mathbf{n} + \mathbf{N}_J^T \mathbf{N}_I \mathbf{n}), \quad (52)$$

for $I, J \in \mathbb{J} \times \mathbb{J}$ and with $\alpha_1 = -4\mu(\lambda + \mu)/(\lambda + 2\mu)$ and $\alpha_2 = 4\mu$. The first-order derivative of \mathbf{r} with respect to \mathbf{n} is given by

$$[K(\mathbf{n})] = \frac{\mathbf{r}(\mathbf{n}) \otimes \mathbf{r}(\mathbf{n})}{\det([\tilde{\pi}(\mathbf{n})])} - \det([\tilde{\pi}(\mathbf{n})]) \frac{\partial [\pi(\mathbf{n})]}{\partial \mathbf{n}} : \left([\tilde{\pi}(\mathbf{n})]^{-1} \boxtimes [\tilde{\pi}(\mathbf{n})]^{-1} \right) : \frac{\partial [\pi(\mathbf{n})]}{\partial \mathbf{n}} + [\text{adj}([\tilde{\pi}(\mathbf{n})])] : \frac{\partial^2 [\pi(\mathbf{n})]}{\partial \mathbf{n} \otimes \partial \mathbf{n}}, \quad (53)$$

where the second-order partial derivatives of $[\pi(\mathbf{n})]$ are given by

$$\frac{\partial^2 \pi_{IJ}(\mathbf{n})}{\partial \mathbf{n} \otimes \partial \mathbf{n}} = \alpha_1 (\mathbf{N}_I \mathbf{n} + \mathbf{N}_I^T \mathbf{n}) \otimes (\mathbf{N}_J \mathbf{n} + \mathbf{N}_J^T \mathbf{n}) + \alpha_1 (\mathbf{N}_J \mathbf{n} + \mathbf{N}_J^T \mathbf{n}) \otimes (\mathbf{N}_I \mathbf{n} + \mathbf{N}_I^T \mathbf{n}) + \alpha_1 \langle \mathbf{n}, \mathbf{N}_I \mathbf{n} \rangle \times (\mathbf{N}_J + \mathbf{N}_J^T) + \alpha_1 \langle \mathbf{n}, \mathbf{N}_J \mathbf{n} \rangle (\mathbf{N}_I + \mathbf{N}_I^T) + \alpha_2 (\mathbf{N}_I^T \mathbf{N}_J + \mathbf{N}_J^T \mathbf{N}_I). \quad (54)$$

Since the normal vector \mathbf{n} is normalized, it can be expressed in terms of polar θ_1 and azimuthal θ_2 angles as $\mathbf{n} = \hat{\mathbf{n}}(\theta)$ with $\hat{\mathbf{n}}(\theta) = (\cos(\theta_1) \sin(\theta_2), \sin(\theta_1) \sin(\theta_2), \cos(\theta_2))$ in the canonical basis of \mathbb{R}^3 . Hence, the minimization problem can be rewritten as $\det([\hat{\pi}(\theta^*)] - [\chi] - [H]) = \min_{\theta \in \Theta} \det([\hat{\pi}(\theta)] - [\chi] - [H])$, (55)

with $[\hat{\pi}(\theta)] = [\pi(\hat{\mathbf{n}}(\theta))]$. Using the chain rule, the associated residual vector $\hat{\mathbf{R}} : \Theta \rightarrow \mathbb{R}^3$ is given by

$$\hat{R}_i(\theta) = D_{ij}(\theta)^T R_j(\hat{\mathbf{n}}(\theta)), \quad D_{ij}(\theta) = \frac{\partial \hat{n}_i(\theta)}{\partial \theta_j}. \quad (56)$$

The problem of finding $\theta \in \Theta$ such that $\hat{\mathbf{R}}(\theta) = \mathbf{0}$ is solved with a Newton–Raphson scheme. Given an initial guess $\theta^{(0)} \in \Theta$, let $\theta^{(k)}$ for $k \geq 1$ be a sequence such that

$$k \geq 0 : \quad [\hat{K}(\theta^{(k)})] (\theta^{(k+1)} - \theta^{(k)}) = -\hat{\mathbf{R}}(\theta^{(k)}), \quad (57)$$

where the tangent matrix $[\hat{K}]$ is given component-wise by

$$\hat{K}_{ij}(\theta) = D_{ik}^T(\theta) K_{kl}(\hat{\mathbf{n}}(\theta)) D_{lj}(\theta) + \hat{R}_k(\theta) \frac{\partial D_{ki}(\theta)}{\partial \theta_j}. \quad (58)$$

Loss of ellipticity is detected at each gauss point of the finite element using the Newton–Raphson procedure given by Eq. (57). In practice, a set of initial guesses $\{\theta^{(0,s)}\}_{s=1}^M$ is first computed by discretization of the unit sphere. The minimization problem is solved for each element of this set and the solution $\theta^{*,s}$ that leads to the lowest indicator $\det([\pi(\hat{\mathbf{n}}(\theta^{*,s}))] - [\chi] - [H])$ is used to determine if ellipticity is lost at the considered Gauss point. Using the solution for the normal vector, \mathbf{n}^* , the determinant of the acoustic tensor can be obtained using the relations

$$\det(\mathbf{Q}_{\text{ep}}^{(0)}(\mathbf{n}^*)) = \det(\mathbf{Q}_{\text{el}}(\mathbf{n}^*)) \det(\mathbf{Q}_{\text{ep}}^{(0)}(\mathbf{n}^*)), \quad \det(\mathbf{Q}_{\text{ep}}^{(0)}(\mathbf{n}^*)) = \det([1] - [G]^{-1} [\pi(\mathbf{n}^*)]), \quad (59)$$

with $\det(\mathbf{Q}_{el}(\mathbf{n})) = (\lambda + 2\mu)\mu^2$ for any normal vector \mathbf{n} . It should be noted that this analysis relies on the tangent elasto-plastic tensor \mathbb{C}^{ep} in the strong formulation of the boundary value problem (see Eqs. (21) and (22)). In the case of numerical simulations involving the finite element method and an implicit discretization scheme, the classical loss of ellipticity analysis of the discretized boundary value problem can also be achieved by considering the algorithmic acoustic tensor (Benallal et al., 2010). The numerical procedures presented by Mosler (2005) and Al Kotob et al. (2019) can be used for loss of ellipticity analysis of the continuum and discretized boundary value problems.

4. Family of linear yield criteria in principal stress space

In this work, we focus on a family of yield functions first introduced by Larsson and Runesson (1996) as a family of generalized Mohr–Coulomb criteria, *i.e.*, a yield function that is a linear combination of the principal stresses. For instance, the Tresca yield function which assumes that yielding takes place when the shear stress reaches a maximum value, belongs to such a family. The twin shear stress model of Yu (1983) and the more recent mean influence factor model of Zhang et al. (2020) also consider yield functions that depend linearly on the principal stresses. The maximum and minimum eigenvalues, σ_1 and σ_3 , are defined as

$$\begin{aligned} \sigma_1(\boldsymbol{\sigma}) &= \max\{\langle \mathbf{z}, \boldsymbol{\sigma} \mathbf{z} \rangle \mid \mathbf{z} \in \mathbb{R}^3, \|\mathbf{z}\| = 1\}, \quad \sigma_3(\boldsymbol{\sigma}) \\ &= \min\{\langle \mathbf{z}, \boldsymbol{\sigma} \mathbf{z} \rangle \mid \mathbf{z} \in \mathbb{R}^3, \|\mathbf{z}\| = 1\}. \end{aligned} \quad (60)$$

The intermediate eigenvalue $\sigma_2(\boldsymbol{\sigma})$ is given by $\sigma_2(\boldsymbol{\sigma}) = \text{Tr}(\boldsymbol{\sigma}) - \sigma_1(\boldsymbol{\sigma}) - \sigma_3(\boldsymbol{\sigma})$ and hence $\sigma_1(\boldsymbol{\sigma}) \geq \sigma_2(\boldsymbol{\sigma}) \geq \sigma_3(\boldsymbol{\sigma})$. By invoking the spectral theorem, the Cauchy stress tensor admits the decomposition

$$\begin{aligned} \boldsymbol{\sigma} &= \sigma_1(\boldsymbol{\sigma}) \mathbf{m}_1(\boldsymbol{\sigma}) \otimes \mathbf{m}_1(\boldsymbol{\sigma}) + \sigma_2(\boldsymbol{\sigma}) \mathbf{m}_2(\boldsymbol{\sigma}) \otimes \mathbf{m}_2(\boldsymbol{\sigma}) \\ &+ \sigma_3(\boldsymbol{\sigma}) \mathbf{m}_3(\boldsymbol{\sigma}) \otimes \mathbf{m}_3(\boldsymbol{\sigma}), \end{aligned} \quad (61)$$

where $\mathbf{m}_1, \mathbf{m}_2$, and \mathbf{m}_3 are the eigenvectors associated to the ordered principal stresses. When no confusion can be made, the dependence of the principal stresses and principal directions on the stress tensor will be dropped. We further introduce a vector-valued parameter $\mathbf{a} = (a_1, a_2, a_3)$ that takes its values in a subset \mathcal{C} of \mathbb{R}^3 to be defined, and such that

$$\sum_{i=1}^3 a_i = 0. \quad (62)$$

We consider the following yield function that is linear in the principal stresses:

$$\phi(\boldsymbol{\sigma}, R) = a_1 \sigma_1(\boldsymbol{\sigma}) + a_2 \sigma_2(\boldsymbol{\sigma}) + a_3 \sigma_3(\boldsymbol{\sigma}) - R. \quad (63)$$

Using Eq. (62), it can readily be deduced that ϕ is pressure insensitive, $\phi(\boldsymbol{\sigma} + q\mathbf{1}) = \phi(\boldsymbol{\sigma})$ for any $q \in \mathbb{R}$. Due to this property, the yield function depends on only two independent parameters. In addition, it should be noted that the parameter $\mathbf{a} = (a_1, a_2, a_3)$ takes its values in a subset \mathcal{C}_{conv} of \mathbb{R}^3 that ensures the convexity of the yield function. The functions $\boldsymbol{\sigma} \mapsto \sigma_1(\boldsymbol{\sigma})$ and $\boldsymbol{\sigma} \mapsto (-\sigma_3(\boldsymbol{\sigma}))$ are both convex but the intermediate principal stress $\boldsymbol{\sigma} \mapsto \sigma_2(\boldsymbol{\sigma})$ is neither convex nor concave. Hence, in the following we shall restrict ourselves to an admissible set of the form $\mathcal{C} = \mathcal{C}_{conv} \cap \mathcal{C}_{inc}$, where

$$\begin{aligned} \mathcal{C}_{conv} &= \{\mathbf{a} \in \mathbb{R}^3 \mid a_1 > a_2 > a_3, a_1 > 0, a_3 < 0\}, \quad \mathcal{C}_{inc} \\ &= \{\mathbf{a} \in \mathbb{R}^3 \mid a_1 + a_2 + a_3 = 0\}, \end{aligned} \quad (64)$$

for the parameter \mathbf{a} . For simplicity, three particular cases will be highlighted in the sequel of this paper, namely:

(C1) Case of the Tresca model obtained for $a_1 = 1, a_2 = 0$, and $a_3 = -1$, that is

$$\phi^{(0)}(\boldsymbol{\sigma}, R) \equiv \sigma_1(\boldsymbol{\sigma}) - \sigma_3(\boldsymbol{\sigma}) - R. \quad (65)$$

(C2) Case of a modified Tresca model obtained for $a_1 = 1, a_2 = -\delta, a_3 = -1 + \delta$, *i.e.*,

$$\phi^{(\delta)}(\boldsymbol{\sigma}, R) \equiv \sigma_1(\boldsymbol{\sigma}) - \delta \sigma_2(\boldsymbol{\sigma}) - (1 - \delta) \sigma_3(\boldsymbol{\sigma}) - R. \quad (66)$$

with $-1 < \delta < 1/2$. This model will be referred to as the δ -Tresca model.

(C3) Case of a modified Tresca model obtained for $a_1 = 1 - \tau, a_2 = \tau$, and $a_3 = -1$, yielding

$$\phi^{(\tau)}(\boldsymbol{\sigma}, R) \equiv (1 - \tau) \sigma_1(\boldsymbol{\sigma}) + \tau \sigma_2(\boldsymbol{\sigma}) - \sigma_3(\boldsymbol{\sigma}) - R, \quad (67)$$

with $-1 < \tau < 1/2$. This model will be referred to as the τ -Tresca model.

These models are illustrated by sketches of the elastic domain in Fig. 1 for different values of δ and τ . It can be seen that the parameter δ (resp. τ) allows for displacing the left corner (resp. right corner) along the hexagone's axes. A combination of these parameterizations results in simultaneous displacements of both corners. It should be noted that given the assumption of ordered principal stresses, the yield functions $\phi^{(\delta)}$ and $\phi^{(\tau)}$ are distinct and only the first sextants of the elastic domains depicted in Fig. 1 are relevant. The twin shear stress model Yu (1983) can also be recovered by considering the yield function $\phi^{(\delta)}$ with $\delta = 1/2$ (resp. $\phi^{(\tau)}$ with $\tau = 1/2$) as the yield function if $\sigma_2 \leq (\sigma_1 + \sigma_3)/2$ (resp. if $\sigma_2 \geq (\sigma_1 + \sigma_3)/2$), that is to say,

$$\phi^{(TSS)} = \begin{cases} \sigma_1 - \frac{1}{2}(\sigma_2 + \sigma_3) - R, & \sigma_2 \leq \frac{1}{2}(\sigma_1 + \sigma_3), \\ \frac{1}{2}(\sigma_1 + \sigma_2) - \sigma_3 - R, & \sigma_2 \geq \frac{1}{2}(\sigma_1 + \sigma_3). \end{cases} \quad (68)$$

Similarly, the recent mean influence factor model Zhang et al. (2020) can be recovered by taking $\delta = (1 - 2\sqrt{3} + \sqrt{13})/4$ and $\tau = (1 - 2\sqrt{3} + \sqrt{13})/4$.

4.1. Flow rule associated to the family of linear yield functions in principal stress space

In this section, we briefly determine the flow rule associated to the yield function defined by Eq. (63) for arbitrary values of the parameter \mathbf{a} . Given that the mapping $g \mapsto \phi(\cdot, R)$ is continuously differentiable, the flow rule (9) reduces to

$$\dot{\boldsymbol{\sigma}}^p \in \dot{\gamma} \partial \varphi(\boldsymbol{\sigma}), \quad \dot{p} = \dot{\gamma} \frac{\partial \phi(\boldsymbol{\sigma}, R)}{\partial R}, \quad (69)$$

where φ is the canonical yield function defined as

$$\varphi(\boldsymbol{\sigma}) = a_1 \sigma_1(\boldsymbol{\sigma}) + a_2 \sigma_2(\boldsymbol{\sigma}) + a_3 \sigma_3(\boldsymbol{\sigma})$$

and its subdifferential is defined as

$$\partial \varphi(\boldsymbol{\sigma}) = \{\mathbf{A} \in \mathcal{P} \mid \phi(\tilde{\boldsymbol{\sigma}}, R) \geq \phi(\boldsymbol{\sigma}, R) + \mathbf{A} : (\tilde{\boldsymbol{\sigma}} - \boldsymbol{\sigma}), \forall \tilde{\boldsymbol{\sigma}} \in \mathcal{S}\}. \quad (70)$$

An explicit expression of the above subdifferential set is reported in A. Such an expression extends existing results for the Tresca and Mohr–Coulomb criteria obtained by He et al. (2005) and Sysala et al. (2017), respectively. In addition, it can be used to derive an implicit integration scheme but this is out of scope of this paper and left for further work. The yield function ϕ is differentiable whenever the principal stresses are distinct, *i.e.*, $\sigma_1(\boldsymbol{\sigma}) > \sigma_2(\boldsymbol{\sigma}) > \sigma_3(\boldsymbol{\sigma})$, while it is subdifferentiable whenever $\sigma_1(\boldsymbol{\sigma}) = \sigma_2(\boldsymbol{\sigma}) \geq \sigma_3(\boldsymbol{\sigma})$ or $\sigma_1(\boldsymbol{\sigma}) \geq \sigma_2(\boldsymbol{\sigma}) = \sigma_3(\boldsymbol{\sigma})$. For further developments, we introduce the following subsets of stresses. The boundary of the elastic domain is denoted by ∂E and decom-

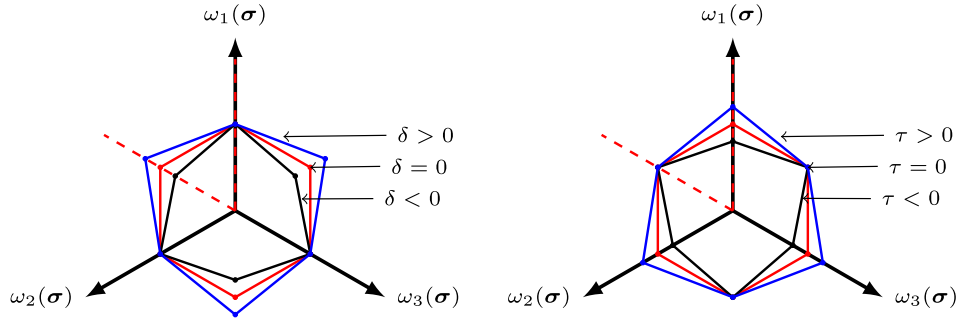


Fig. 1. Elastic domains in the deviatoric plane for different values of the parameters δ and τ . The classical Tresca model (in red) is recovered for $\delta = 0$ (or $\tau = 0$) while $\delta \neq 0$ and $\tau \neq 0$ modify the positions of the left and right corners along the hexagone's axes. Here, $\omega_1(\boldsymbol{\sigma}), \omega_2(\boldsymbol{\sigma}), \omega_3(\boldsymbol{\sigma})$ denote the eigenvalues of the stress tensor $\boldsymbol{\sigma}$ without particular ordering. (For interpretation of the references to colour in this figure legend, the reader is referred to the web version of this article.)

posed as a union of disjoint sets $\partial E = \partial E_l \cup \partial E_s \cup \partial E_r$. These sets correspond to the left corner, smooth portion, and right corner of the yield surface, that is

$$\partial E_l = \{\boldsymbol{\sigma} \in \partial E \mid \sigma_1(\boldsymbol{\sigma}) - \sigma_2(\boldsymbol{\sigma}) = 0, \sigma_2(\boldsymbol{\sigma}) \geq \sigma_3(\boldsymbol{\sigma})\}, \quad (71a)$$

$$\partial E_s = \{\boldsymbol{\sigma} \in \partial E \mid \sigma_1(\boldsymbol{\sigma}) > \sigma_2(\boldsymbol{\sigma}) > \sigma_3(\boldsymbol{\sigma})\}, \quad (71b)$$

$$\partial E_r = \{\boldsymbol{\sigma} \in \partial E \mid \sigma_1(\boldsymbol{\sigma}) \geq \sigma_2(\boldsymbol{\sigma}), \sigma_2(\boldsymbol{\sigma}) - \sigma_3(\boldsymbol{\sigma}) = 0\}. \quad (71c)$$

The subsets given by Eq. (71) are illustrated for the δ -Tresca model in Fig. 2. These definitions hold for any vector-valued parameter $\mathbf{a} \in \mathcal{C}$ and thus for the three particular cases defined by Eqs.(65)–(67). We focus on the multisurface form of flow rule in order to use the loss of ellipticity conditions summarized in Section 3. For this purpose, it can be noticed that the elastic domain can also be defined in terms of the following three yield functions

$$\begin{aligned} \phi_1(\boldsymbol{\sigma}, R) &= a_1 \sigma_1(\boldsymbol{\sigma}) + a_2 \sigma_2(\boldsymbol{\sigma}) + a_3 \sigma_3(\boldsymbol{\sigma}) - R, \\ \phi_2(\boldsymbol{\sigma}, R) &= a_1 \sigma_2(\boldsymbol{\sigma}) + a_2 \sigma_1(\boldsymbol{\sigma}) + a_3 \sigma_3(\boldsymbol{\sigma}) - R, \\ \phi_3(\boldsymbol{\sigma}, R) &= a_1 \sigma_1(\boldsymbol{\sigma}) + a_2 \sigma_3(\boldsymbol{\sigma}) + a_3 \sigma_2(\boldsymbol{\sigma}) - R. \end{aligned} \quad (72)$$

This multisurface representation depends on a single yield stress R and the extension to distinct yield stresses could be considered in a future work. In the sequel of this section, we shall denote by \mathbf{N}_j the second-order tensors defined as $\mathbf{N}_j = \nabla_{\boldsymbol{\sigma}} \phi_j$, that is

$$\begin{aligned} \mathbf{N}_1 &= a_1 \mathbf{m}_1 \otimes \mathbf{m}_1 + a_2 \mathbf{m}_2 \otimes \mathbf{m}_2 + a_3 \mathbf{m}_3 \otimes \mathbf{m}_3, \\ \mathbf{N}_2 &= a_2 \mathbf{m}_1 \otimes \mathbf{m}_1 + a_1 \mathbf{m}_2 \otimes \mathbf{m}_2 + a_3 \mathbf{m}_3 \otimes \mathbf{m}_3, \\ \mathbf{N}_3 &= a_1 \mathbf{m}_1 \otimes \mathbf{m}_1 + a_3 \mathbf{m}_2 \otimes \mathbf{m}_2 + a_2 \mathbf{m}_3 \otimes \mathbf{m}_3. \end{aligned} \quad (73)$$

With the above definitions at hand, the multisurface form of the flow rule takes the form

$$\dot{\boldsymbol{\epsilon}}^p = \sum_{j \in \mathcal{J}} \dot{\gamma}_j \mathbf{N}_j,$$

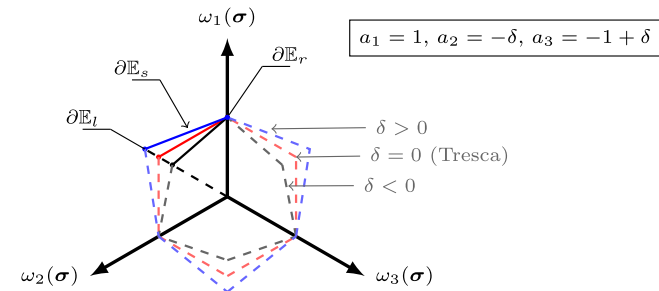


Fig. 2. Elastic domains in the deviatoric plane for different values of the parameter δ together with the subsets $\partial E_l, \partial E_s$, and ∂E_r . Here, $\omega_1(\boldsymbol{\sigma}), \omega_2(\boldsymbol{\sigma}), \omega_3(\boldsymbol{\sigma})$ denote the eigenvalues of the stress tensor $\boldsymbol{\sigma}$ without particular ordering.

where it is recalled that \mathcal{J} denotes the set of active mechanisms. The equivalence between the multisurface and subdifferential-based flow rules is discussed in B based on the developments of Section 2.2.

4.2. Critical hardening moduli

With the yield function and flow rule now clearly defined, we are able to analyze under which circumstances loss of ellipticity may occur. In the sequel of this section, Young's modulus is set to $E = 210$ GPa and unless stated otherwise, the Poisson's ratio is chosen as $\nu = 0.3$. The aim of this section is to determine the critical hardening moduli and the associated normals vector \mathbf{n} to the shear bands. The hardening matrix $[H]$ is assumed to belong to the family defined by Eq. (C.1) with $\ell = 1$. Hence, the evolutions of the internal variable p and the yield radius R (see Eqs.(15)–(18)) reduce to

$$\dot{p} = \sum_{j \in \mathcal{J}} \dot{\gamma}_j, \quad \dot{R} = H \sum_{j \in \mathcal{J}} \dot{\gamma}_j. \quad (74)$$

Three different situations will be considered, namely, a current stress state that lies on the smooth portion, left corner, right corner of the yield surface. For each situation, the three particular cases described in Section 4 (see Fig. 1) will be illustrated. The case of the smooth portion of the yield surface is first studied in Section 4.2.1. The left and right corners are then addressed in Section 4.2.2.

4.2.1. Critical hardening modulus on the smooth portion of the yield surfaces

If the current stress state lies on the smooth portion of the yield surface, $(\boldsymbol{\sigma}, R) \in \partial E_s$, the critical hardening modulus can be obtained using the results presented in Section 3.1. Let k^* be the index defined such that $|a_{k^*}| = \min\{|a_1|, |a_2|, |a_3|\}$. Using Eq. (34), the critical hardening modulus and the associated normal \mathbf{n} are given by

$$\begin{aligned} H_s^{\text{crit}} &= -E a_{k^*}^2, \quad n_{k^*} = 0, \quad n_i^2 = \frac{a_i + \nu a_{k^*}}{a_i - a_j}, \quad n_j^2 \\ &= 1 - n_i^2, \quad i, j \neq k^*. \end{aligned} \quad (75)$$

If $n_i = 1$ and $n_j = n_k = 0$ for any $i \in \{1, 2, 3\}$, then the critical modulus is given by Eq. (36). However, it has been found that this solution yields less favorable critical hardening moduli.

(C1) In the particular case of a Tresca model, that is $a_1 = 1, a_2 = 0$, and $a_3 = -1$, the most favorable critical hardening modulus $H_{0,s}^{\text{crit}}$ and the normal vector $\mathbf{n}_{0,s}^{\text{crit}}$ are given by

$$H_{0,s}^{\text{crit}} = 0, \quad \mathbf{n}_{0,s}^{\text{crit}} = \frac{1}{\sqrt{2}} \begin{bmatrix} \pm 1 \\ 0 \\ \pm 1 \end{bmatrix}_{(\mathbf{m}_i)_{i=1}^3}, \quad (76)$$

meaning that the shear band is oriented with a 45° angle in the plane spanned by $(\mathbf{m}_1, \mathbf{m}_3)$.

(C2) In the case of the δ -Tresca model, it is found that $a_{k^*} = a_2$ and thus $a_{k^*} = -\delta$ for any $\delta \in]-1, 1/2[$. The first possible critical hardening modulus is given by $H_{\delta,s}^{\text{crit}} = -E\delta^2$ and the associated normal vector $\mathbf{n}_{\delta,s}^{\text{crit}}$ can be written as $\mathbf{n}_{\delta,s}^{\text{crit}} = (\cos(\theta), 0, \sin(\theta))$ in the principal stress basis. In summary, the following solutions are found for the critical hardening modulus and the normal vector:

$$H_{\delta,s}^{\text{crit}} = -E\delta^2, \quad (77)$$

$$\mathbf{n}_{\delta,s}^{\text{crit}} = \frac{1}{\sqrt{2-\delta}} \begin{bmatrix} \pm\sqrt{1-v\delta} \\ 0 \\ \pm\sqrt{1-\delta(1-v)} \end{bmatrix}_{(\mathbf{m}_i)_{i=1}^3} \quad \text{or} \quad (78)$$

$$\mathbf{n}_{\delta,s}^{\text{crit}} = \frac{1}{\sqrt{2-\delta}} \begin{bmatrix} \pm\sqrt{1-\delta(1-v)} \\ 0 \\ \pm\sqrt{1-v\delta} \end{bmatrix}_{(\mathbf{m}_i)_{i=1}^3}.$$

Graphs of the mappings $\delta \mapsto \theta_1(\delta)$ and $\delta \mapsto \theta_2(\delta)$ associated to the above normal vectors are shown in Fig. 3 for selected values of Poisson's ratio $v \in [0.1, 0.5]$. It can easily be verified that $1 - v\delta > 0$ and $1 - \delta(1 - v) > 0$ for any $v \in [0, 0.5]$ and $\delta \in]-1, 1/2[$.

(C3) In the case of the τ -Tresca model with $a_1 = 1 - \tau, a_2 = \tau, a_3 = -1$, one has $a_{k^*} = \tau$. Similarly to Eq. (77), it follows that the critical hardening modulus $H_{\tau,s}^{\text{crit}}$ is given by

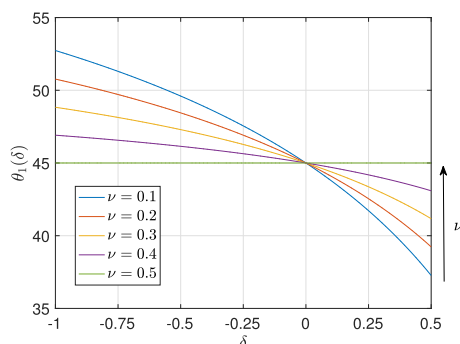
$$H_{\tau,s}^{\text{crit}} = -E\tau^2, \quad (79)$$

and the possible normal vectors take the forms

$$\mathbf{n}_{\tau,s}^{\text{crit}} \frac{1}{\sqrt{2-\tau}} = \begin{bmatrix} \pm\sqrt{1-\tau(1-v)} \\ 0 \\ \pm\sqrt{1-v\tau} \end{bmatrix}_{(\mathbf{m}_i)_{i=1}^3} \quad \text{or} \quad (80)$$

$$\mathbf{n}_{\tau,s}^{\text{crit}} = \frac{1}{\sqrt{2-\tau}} \begin{bmatrix} \pm\sqrt{1-v\tau} \\ 0 \\ \pm\sqrt{1-\tau(1-v)} \end{bmatrix}_{(\mathbf{m}_i)_{i=1}^3}.$$

Similar graphs of the associated angles θ_1 and θ_2 are obtained as those given by the right and left panel of Fig. 3, respectively. From the previous developments, it follows that



$$1 - v\tau > 0 \quad \text{and} \quad 1 - \tau(1 - v) > 0 \quad \text{for any } v \in [0, 0.5] \quad \text{and} \quad \tau \in]-1, 1/2[.$$

As a result, it can be deduced that the standard Tresca model leads to the largest critical hardening modulus whenever the stress tensor lies on the smooth portion of the yield surface. In the next section, the same analysis is performed on the corners of the yield surface.

4.2.2. Critical hardening moduli on the corners of the yield surface

If the current stress state lies on a corner of the yield surface, then the critical hardening modulus can be obtained using the developments of Section 3.2. In this section, we first assume that the stress state lies on the right corner (see Eq. (71) and Fig. 2). In this case, the set of active mechanisms \mathbb{J} is given by $\mathbb{J} = \{1, 3\}$. The hardening matrix $[H_r]$ denotes the restriction of $[H]$ when the stresses lie on the right corner of the yield surface, i.e.,

$$[H_r] = H[i_2], \quad [i_2] = \begin{bmatrix} 1 & 1 \\ 1 & 1 \end{bmatrix}. \quad (81)$$

The matrix $[\tilde{G}]$ involved in Eq. (42) takes the form

$$[\tilde{G}] = [\tilde{\chi}] + [H_r] \quad \text{where} \quad (82)$$

$$[\tilde{\chi}] = \begin{bmatrix} \mathbf{N}_1 : \mathbb{C} : \mathbf{N}_1 & \mathbf{N}_1 : \mathbb{C} : \mathbf{N}_3 \\ \mathbf{N}_3 : \mathbb{C} : \mathbf{N}_1 & \mathbf{N}_3 : \mathbb{C} : \mathbf{N}_3 \end{bmatrix} =$$

$$2\mu \begin{bmatrix} a_1^2 + a_2^2 + a_3^2 & a_1^2 + 2a_2a_3 \\ a_1^2 + 2a_2a_3 & a_1^2 + a_2^2 + a_3^2 \end{bmatrix}.$$

Let N_i^k, N_i^l and n_i be the components of $\mathbf{N}_k, \mathbf{N}_l$, and \mathbf{n} in the principal stress basis $(\mathbf{m}_1, \mathbf{m}_2, \mathbf{m}_3)$. From Eq. (40), it is deduced that the entries of the matrix $[\pi(\mathbf{n})]$ on an arbitrary corner can be written as $\hat{\pi}_{ij}(n_1, n_2, n_3) = \pi_{ij}(\mathbf{n})$ with

$$\hat{\pi}_{ij}(n_1, n_2, n_3) = -\frac{4\mu(\lambda + \mu)}{\lambda + 2\mu} \sum_{i=1}^3 n_i^2 N_i^k \sum_{j=1}^3 n_j^2 N_j^l$$

$$+ 4\mu \sum_{i=1}^3 N_i^k N_i^l n_i^2, \quad \mathbf{n}$$

$$= \sum_{k=1}^3 n_k \mathbf{m}_k. \quad (83)$$

On the right corner of the yield surface, the eigenvalues of \mathbf{N}_1 and \mathbf{N}_3 are given by (a_1, a_2, a_3) and (a_1, a_3, a_2) , respectively. For brevity, the entries (83) for an arbitrary normal vector \mathbf{n} are not listed herein. Given the matrices $[\pi(\mathbf{n})]$ and $[\tilde{\chi}]$, the critical hardening modulus can be computed via Eq. (46) provided that

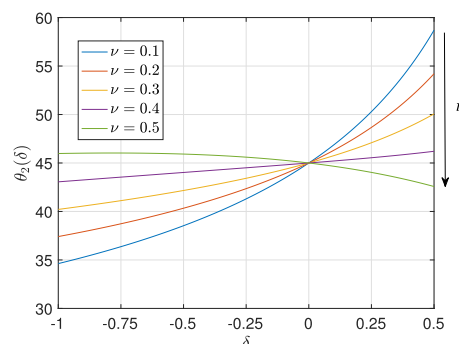


Fig. 3. Graphs of the angles $\delta \mapsto \theta_1(\delta)$ and $\delta \mapsto \theta_2(\delta)$ formed by the two possible normal vectors to the shear band on the smooth portion of the yield surface, and depending on the value of the Poisson ratio.

$[\boldsymbol{\pi}(\mathbf{n})] - [\tilde{\boldsymbol{\chi}}]$ is non-singular. However, for selected normal vectors \mathbf{n} listed below, it is found that $[\boldsymbol{\pi}(\mathbf{n})] - [\tilde{\boldsymbol{\chi}}]$ is singular and thus non-invertible. For these selected normals, closed-form expressions of the determinant of $[\boldsymbol{\pi}(\mathbf{n})] - [\tilde{\boldsymbol{G}}]$ can be obtained:

$$\det([\boldsymbol{\pi}(\mathbf{n})] - [\tilde{\boldsymbol{G}}]) = H\mu \frac{3\lambda + 5\mu}{\lambda + 2\mu} (a_1 + 2a_3)^2, \quad \text{if } n_1^2 = n_2^2 = \frac{1}{2}, \quad n_3 = 0, \quad (84a)$$

$$\det([\boldsymbol{\pi}(\mathbf{n})] - [\tilde{\boldsymbol{G}}]) = H\mu \frac{3\lambda + 5\mu}{\lambda + 2\mu} (a_1 + 2a_3)^2, \quad \text{if } n_1^2 = n_3^2 = \frac{1}{2}, \quad n_2 = 0, \quad (84b)$$

$$\det([\boldsymbol{\pi}(\mathbf{n})] - [\tilde{\boldsymbol{G}}]) = 0, \quad \text{if } n_2^2 = n_3^2 = \frac{1}{2}, \quad n_1 = 0. \quad (84c)$$

It follows that the hardening modulus $H: \mathbf{n} \mapsto \mathbb{R}$ such that $\det([\boldsymbol{\pi}(\mathbf{n})] - [\tilde{\boldsymbol{\chi}}] - H(\mathbf{n})[i_2]) = 0$ is given by

$$H(\mathbf{n}) = \begin{cases} 0, & \text{if } n_1^2 = n_2^2 = \frac{1}{2}, \quad n_3 = 0, \\ 0, & \text{if } n_1^2 = n_3^2 = \frac{1}{2}, \quad n_2 = 0, \\ h \in \mathbb{R}, & \text{if } n_2^2 = n_3^2 = \frac{1}{2}, \quad n_1 = 0, \\ \left(([\boldsymbol{\pi}(\mathbf{n})] - [\tilde{\boldsymbol{\chi}}])^{-1} : [i_2] \right)^{-1}, & \text{else.} \end{cases} \quad (85)$$

Fig. 4 shows the graph of $\mathbf{n} \mapsto H(\mathbf{n})$ for normal vectors \mathbf{n} such that $\mathbf{n} = (\cos(\theta), 0, \sin(\theta))$ or $\mathbf{n} = (\cos(\theta), \sin(\theta), 0)$. It is found that this hardening modulus only depends on a_1 amongst the three parameters a_1, a_2 , and a_3 . Left panel of Fig. 5 shows graphs of the determinant of the normalized acoustic tensor $\mathbf{Q}_{ep}^{(0)}$ for stresses on the right corner of the yield surface with respect to the normalized hardening modulus $H(\mathbf{n}) \times E^{-1}$. The right panel of Fig. 5 shows the minimum value of the same determinant obtained with the algorithm described in Section 3.3. It follows that the critical hardening modulus H_r^{crit} and the associated normal \mathbf{n}_r^{crit} defined such that it yields a singular acoustic tensor $\mathbf{Q}_{ep}^{(0)}$ is given by

$$H_r^{crit} \in \left[0, +\infty \right], \quad \mathbf{n}_r^{crit} = \begin{cases} \pm \frac{1}{\sqrt{2}}(\mathbf{m}_2 \pm \mathbf{m}_3), & \text{if } H_r \geq 0, \\ \pm \frac{1}{\sqrt{2}}(\mathbf{m}_1 \pm \mathbf{m}_2) \text{ or } \pm \frac{1}{\sqrt{2}}(\mathbf{m}_1 \pm \mathbf{m}_3), & \text{if } H_r = 0, \end{cases} \quad (86)$$

where the eigenvectors \mathbf{m}_2 and \mathbf{m}_3 are arbitrary unit vectors orthogonal to \mathbf{m}_1 . Similar results are obtained for stresses on the

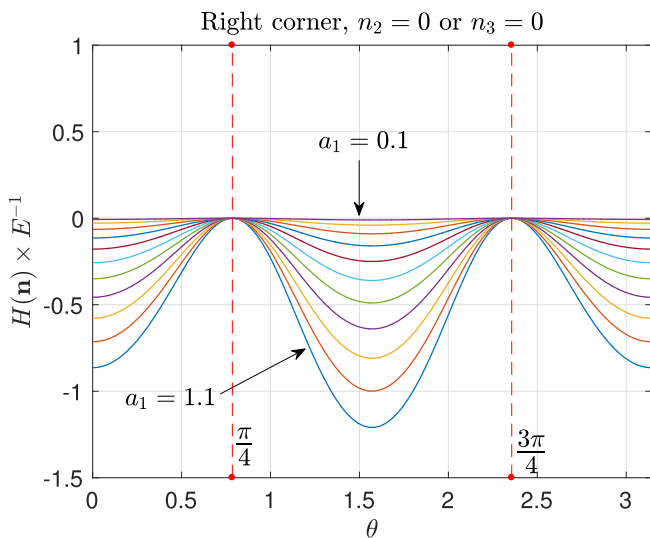


Fig. 4. Graph of the hardening modulus $\mathbf{n} \mapsto H(\mathbf{n})$ such that $\det([\boldsymbol{\pi}(\mathbf{n})] - [\tilde{\boldsymbol{\chi}}] - H(\mathbf{n})[i_2]) = 0$ for selected families of the normal vectors \mathbf{n} a few values of $a_1 > 0$.

left corner of the yield surface. The critical hardening modulus H_r^{crit} and the associated normal vector \mathbf{n}_r^{crit} are found to be such that

$$H_r^{crit} \in \left[0, +\infty \right], \quad \mathbf{n}_r^{crit} = \begin{cases} \pm \frac{1}{\sqrt{2}}(\mathbf{m}_1 \pm \mathbf{m}_2), & \text{if } H_l \geq 0, \\ \pm \frac{1}{\sqrt{2}}(\mathbf{m}_2 \pm \mathbf{m}_3) \text{ or } \pm \frac{1}{\sqrt{2}}(\mathbf{m}_1 \pm \mathbf{m}_3), & \text{if } H_l = 0. \end{cases} \quad (87)$$

As a result, on the corners of the yield surface, the linearized loss of ellipticity condition (27) and the condition (42) are fulfilled for any positive hardening modulus. In addition, the condition (28) is fulfilled for any strictly negative hardening modulus, i.e., for softening behaviors.

5. Numerical examples

In this section, finite element simulations are performed in order to illustrate the proposed analysis. For simplicity, only the δ -Tresca model will be considered. Three different geometries are introduced, namely, a cube in Section 5.1, and a thin plate that measures $L = 12$ mm in height, $L/3$ mm in width, and is $L/6$ mm thick in Section 5.2. Finally, an experimental tubular specimen is considered in Section 5.3. The geometries are discretized with 20-noded hexahedral elements and a reduced integration scheme is used within each element to reduce locking phenomena. Finite element meshes of the geometries are shown in Fig. 6. Finite element simulations are performed with the non-linear material and structure analysis suite Zset (<http://zset-software.com/>). A nonlinear hardening function $\hat{p} \mapsto R(\hat{p})$ is chosen as

$$R(\hat{p}) = R_0 + S\hat{p} + Q(1 - \exp(-b\hat{p})),$$

for which the hardening modulus $\hat{p} \mapsto H(\hat{p}) \equiv dR(\hat{p})/d\hat{p}$ takes the form

$$H(\hat{p}) = S + Qb \exp(-b\hat{p}). \quad (88)$$

In the above equations, R_0 is a constant yield stress, Q , and b are two hardening parameters chosen as

$$R_0 = 1000 \text{ MPa}, \quad Q = 100 \text{ MPa}, \quad b = 300$$

and the linear hardening modulus S is given by

$$S = -1000 \text{ MPa}.$$

Young's modulus and Poisson's ratio are set to $E = 210,000$ MPa and $\nu = 0.3$. Imperfections are inserted by imposing a reduced yield stress $R_0' = 999.0$ MPa in chosen elements of the cube and thin plate. The objective of the imperfection is to fix the location of the strain localization band which will form and avoid complex interactions with the boundaries. In the rest of this section, localization and loss of ellipticity are studied for various plastic thresholds and the considered three geometries. The implicit integration scheme used for the time integration of the elasto-plastic constitutive problem is reported in D.

5.1. Softening cube undergoing tension

We start by comparing the results obtained with a cube using the Tresca and von Mises yield functions. A vertical displacement u_d is applied to the top edge and boundary conditions at the bottom of the cube are such that tensile homogeneous deformations take place in the elastic regime. In this setting, we expect the stress state to lie on the right corner of the yield surface at most Gauss points of the finite element mesh. The parameter S in Eq. (88) is chosen as $S = -1000$ MPa in order to enforce a slightly softening behavior.

Fig. 7 shows the reaction forces on the top surface of the cube for six different plastic thresholds, namely, for the von Mises, Tresca, and δ -Tresca model with four different values of the param-

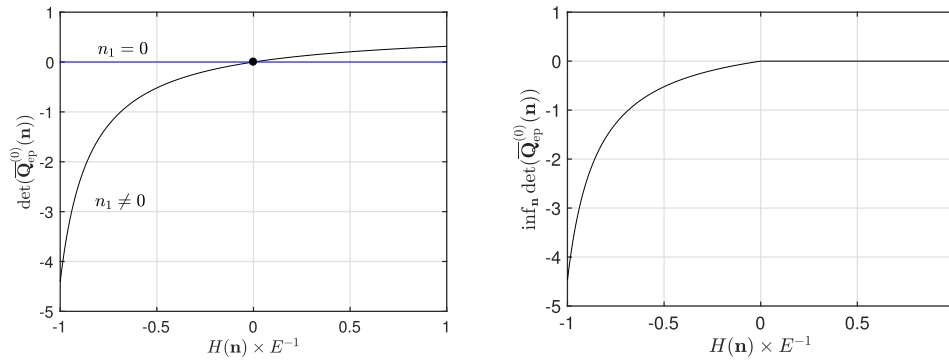


Fig. 5. Graphs of the determinant of normalized the acoustic tensor with respect to the hardening modulus for stresses on the right corner of the yield surface.

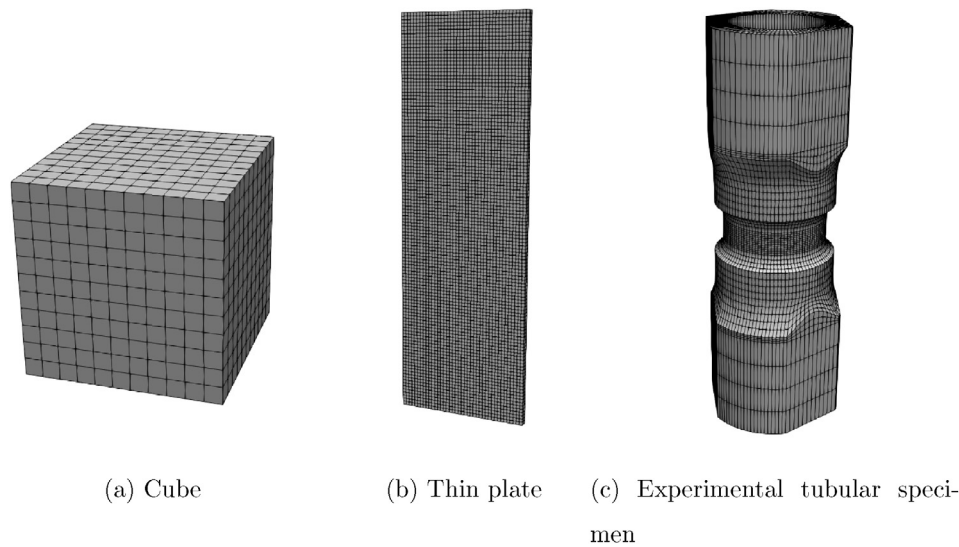


Fig. 6. Finite element meshes of the cube (using 10 elements in each direction) and thin plate (using 80, 240, and 4 quadratic elements along the width, height, and thickness, respectively), and geometry of the tubular specimen taken from (Defaïsse et al., 2018 and Al Kotob et al. (2019)).

eter δ . In addition, in Fig. 7, the prescribed deformation ε_E for which loss of ellipticity occurs for the first time in the finite element mesh is shown. The first occurrence of loss of ellipticity is obtained as follows. At each time step, the minimum of the loss of ellipticity indicator over all the Gauss points is computed. This minimum value is considered to be negative as soon as it gets lower than or equal to -10^{-14} . The prescribed deformation ε_D for which the resultant force reaches its maximum value is also given. In the case of the von Mises model, it is seen that loss of ellipticity occurs well after the resultant force has reached its maximum value. In contrast, in the case of the δ -Tresca models with $\delta \in \{-0.2, -0.1, 0.0, 0.1, 0.2\}$, it is observed that loss of ellipticity occurs slightly before the maximum resultant force. In Fig. 8, the graph of the minimum value of the loss of ellipticity indicator is shown with respect to the prescribed deformation u_d/L . The minimum is taken over all the Gauss points of the finite element mesh. A value equal to 1 means that ellipticity has not decreased. It can be seen that the indicators suddenly decrease as soon as the cube plastifies. In the case of the von Mises model, the indicator drops to a positive value then smoothly decreases. In contrast, in the case of the Tresca model, the indicator directly drops to zero then smoothly decreases towards negative values. This numerical observation can be explained by means of Eq. (86). Indeed, on the right corner of the Tresca yield function, we expect the acoustic tensor to be singular as soon as the material plastifies.

Fig. 9 shows that strain remains almost homogeneous using the von Mises criterion, whereas strain localization bands tend to form according to Tresca and δ -Tresca criteria. The same fields are shown in Fig. 10 in the case of the Tresca model. In contrast to the von Mises model, a distinctive strain localization band forms on the top surface of the cube. The indicator of loss of ellipticity decreases where localization occurs.

It is well-known that loss of ellipticity for von Mises plasticity under tension can only occur for a very low value of softening modulus, namely $-E/4$, as discussed by, e.g., Besson et al. (2009). Here, the presence of an imperfection leads to a heterogeneous deformation field and loss of ellipticity occurs even in the case of the von Mises model. However, it occurs for a much larger prescribed displacement and much higher deformations that are unrealistic under the assumptions of small strains.

5.2. Thin softening plate undergoing tension

In this second illustration, we consider the case of a thin plate. The boundary conditions are the same as in the case of the cube addressed in the previous section, namely, there are such that homogeneous simple tension takes place in the absence of localization. The parameter S in Eq. (88) is chosen as $S = -1000$ MPa as in the previous section. The resultant forces on the top surface of the plate are shown in Fig. 11 for the von Mises and δ -Tresca models.

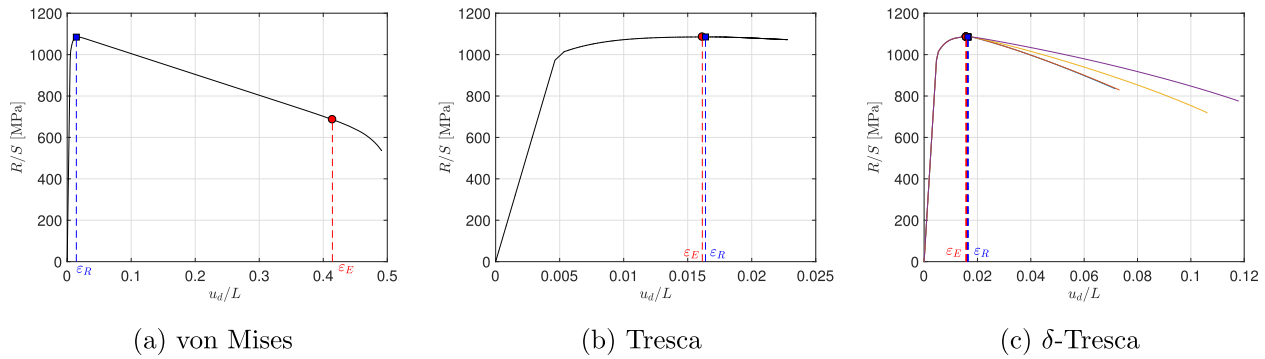


Fig. 7. Cube undergoing simple tension: graphs of the force resultant R with respect to the prescribed deformation u_d/L with $L = 4$ mm. The deformations ε_E and ε_R correspond to: the first occurrence of loss of ellipticity and to when R reaches its maximum value.

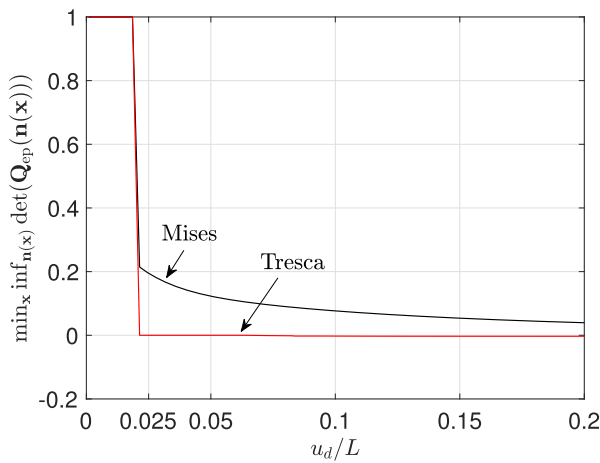


Fig. 8. Cube undergoing simple tension: graph of minimum value of the loss of ellipticity indicator over the Gauss points of the finite element meshes, with respect to the prescribed deformation u_d/L with $L = 4$ mm.

As in the case of the cube, loss of ellipticity occurs late after the resultant force has reached its maximum value for the von Mises model. In contrast, for all the δ -Tresca models, loss of ellipticity takes place slightly before the maximum reaction force. In addition, it can be seen that loss of ellipticity is slightly postponed as δ increases. Views of the cumulative plastic strain field in the case of a Tresca model are shown in Fig. 12. The localization band is found to be inclined across both the thickness and width. To explain this numerical result, we refer to Eq. (86) which shows that on the right corner of the Tresca yield surface, we may have

$$\det(\mathbf{Q}_{ep}(\mathbf{n}(\mathbf{x}))) = 0, \quad \mathbf{n} = \frac{1}{\sqrt{2}} \begin{bmatrix} 0 \\ \pm 1 \\ \pm 1 \end{bmatrix}_{(\mathbf{m}_i)_{i=1}^3}, \quad \forall H(p(\mathbf{x})) \in [0, +\infty[, \quad (89)$$

or

$$\det(\mathbf{Q}_{ep}(\mathbf{n}(\mathbf{x}))) = 0, \quad \mathbf{n}(\mathbf{x}) = \frac{1}{\sqrt{2}} \begin{bmatrix} \pm 1 \\ \pm 1 \\ 0 \end{bmatrix}_{(\mathbf{m}_i)_{i=1}^3} \quad \text{or} \quad (90)$$

$$\mathbf{n}(\mathbf{x}) = \frac{1}{\sqrt{2}} \begin{bmatrix} \pm 1 \\ 0 \\ \pm 1 \end{bmatrix}_{(\mathbf{m}_i)_{i=1}^3},$$

for $H(p(\mathbf{x})) = 0$ at any point \mathbf{x} in deformed configuration. If it is assumed that in this scenario of simple tension the eigenvalues $\{\mathbf{m}_i\}_{i=1}^3$ coincide with the canonical basis $(\mathbf{e}_x, \mathbf{e}_y, \mathbf{e}_z)$ of \mathbb{R}^3 , then Eq. (89) means that a flat shear band across the plate's width may take place as well. Similarly, Eq. (90) states that an inclined shear band in the planes spanned by $(\mathbf{e}_x, \mathbf{e}_y)$ or $(\mathbf{e}_x, \mathbf{e}_z)$ may take place. However, it should be emphasized that the eigenvectors \mathbf{m}_2 and \mathbf{m}_3 can be arbitrary vectors than span the space orthogonal to the linear space $\{\alpha \mathbf{m}_1, \alpha \in \mathbb{R}\}$, hence leading to the observed shear band in Fig. 12. As a comparison, in the case of a von Mises model, the shear band would also be inclined across the plate's width but flat across the thickness of the plate. In the latter case, necking takes place within the thickness of the band and no loss of ellipticity occurs.

To end this section, Fig. 13 shows the loss of ellipticity indicators in the case of various plastic thresholds. Similar results are obtained in most cases expect for the δ -Tresca model with $\delta = -0.2$ and the von Mises model. For the latter, it is not surprising that ellipticity is not lost at $u_d/L \approx 0.0175$ since loss of ellipticity occurs for $u_d/L \geq \varepsilon_E$ with $\varepsilon_E > 0.0175$ (see Fig. 11). In the case of the δ -Tresca model with $\delta = -0.2$, it is found that a flat shear band takes place across the plate's width. We infer that for $\delta = -0.2$, we obtained a shear band orientation \mathbf{n} with entries $n_1 = 0, n_2^2 = n_3^2$ in the principal basis (that may coincide with the canonical basis).

5.3. Experimental tubular specimen undergoing tension and torsion

In this last section, we consider the experimental tubular specimen shown in Fig. 6(c). The objective of this example is to show that the proposed analysis is applicable to realistic experimental samples under complex loading conditions. Three different boundary value problems are considered. The first one consists in a pure torsion test where a relative rotation θ is applied to the top and bottom surfaces. The second configuration is a simple tension test where a vertical displacement is applied to the top surface. And finally, the third scenario is obtained by combining these tension and torsion tests. As in the previous numerical illustrations, a slightly softening behavior is enforced by taking $S = -1000$ MPa (see Eq. (88)). However, in contrast to the previous cases in Sections 5.1 and 5.2, no imperfection is inserted in the finite element mesh. The following subsections comment the finite element simulations displayed in Fig. 15 (pure torsion), Fig. 16 (simple tension), Fig. 17 (combined torsion-tension). All the snapshots were taken at the time-step at which ellipticity is lost for the first time during the simulations. The reader is referred to Fig. 14 where graphs of the resultant moments and forces are shown, together with the first occurrences of loss of ellipticity. The results can be compared to the corresponding experimental data provided by Defaïsse et al.

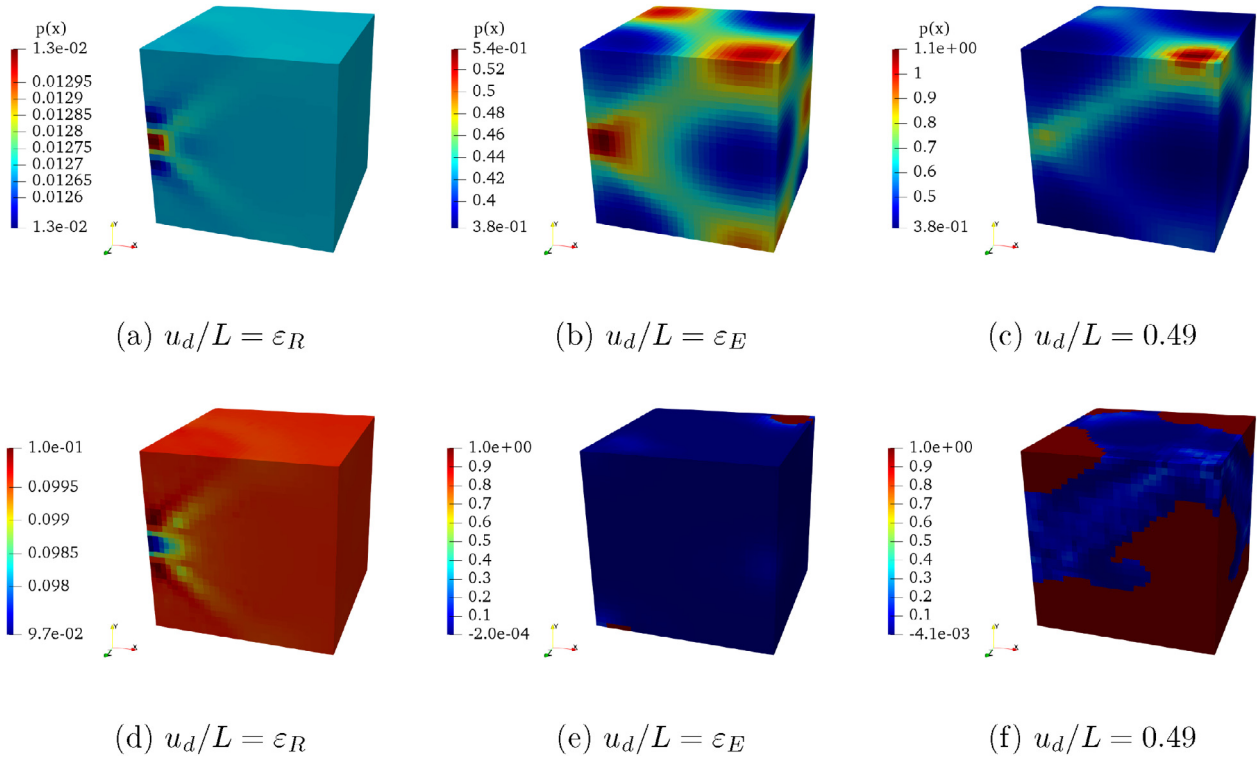


Fig. 9. Cumulative plastic strain $\mathbf{x} \mapsto p(\mathbf{x})$ (first row) and loss of ellipticity indicator $\mathbf{x} \mapsto \inf_{\mathbf{n}(\mathbf{x}) \in \mathcal{S}} \det(\mathbf{Q}_{ep}(\mathbf{n}(\mathbf{x})))$ (second row) in the case of a von Mises model at three overall strain levels indicated in Fig. 7(a).

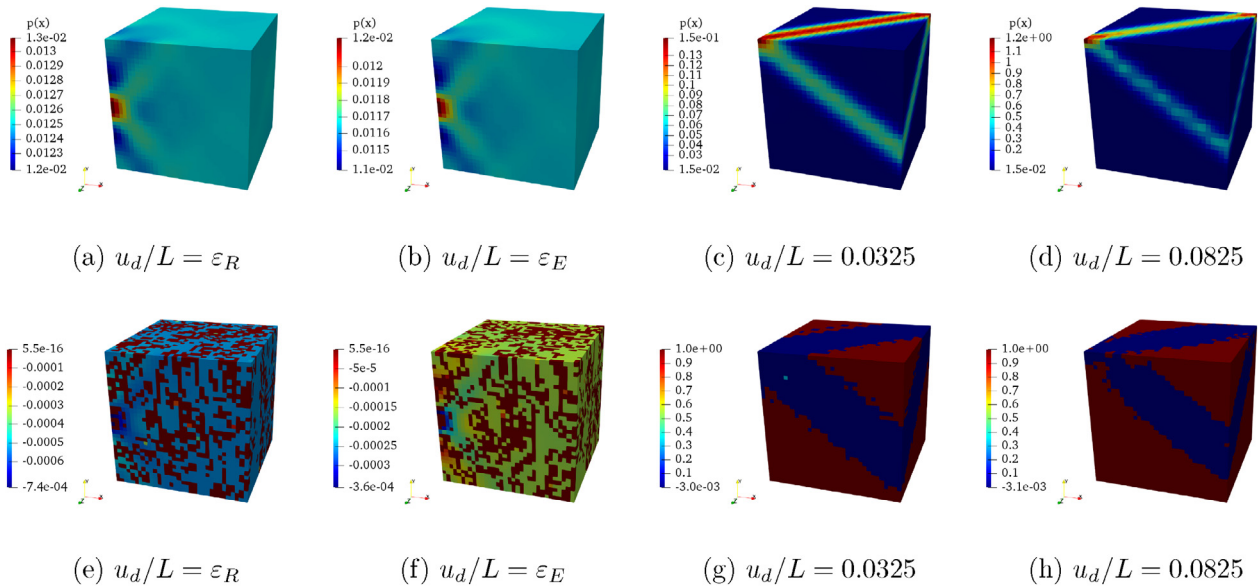


Fig. 10. Cumulative plastic strain $\mathbf{x} \mapsto p(\mathbf{x})$ (first row) and loss of ellipticity indicator $\mathbf{x} \mapsto \inf_{\mathbf{n}(\mathbf{x}) \in \mathcal{S}} \det(\mathbf{Q}_{ep}(\mathbf{n}(\mathbf{x})))$ (second row) in the case of a Tresca model at four overall strain levels indicated in Fig. 7(b).

(2018) for ultra-high strength steel which does not exhibit significant damage prior to shear band localization and final fracture. It is proposed that Tresca-like constitutive models would be more suitable than the standard von Mises criterion to capture these localization events.

5.3.1. Experimental tubular specimen undergoing pure torsion

Graphs of the resultant moment with respect to the rotation angle are shown in the left panel of Fig. 14 in the case of pure tor-

sion, and snapshots of the cumulative plastic strains and loss of ellipticity indicators are provided in Fig. 15. In this scenario, the stress tensor lies on the smooth portion of the δ -Tresca yield surfaces. It can be observed that the Tresca and von Mises models lead to loss of ellipticity almost simultaneously when the resultant moment reaches its maximum value. This is due to the fact that their normals to the yield surfaces and critical hardening moduli coincide in pure shear. In contrast, the δ -Tresca models with $\delta = -0.2$ or $\delta = 0.2$ allow for postponing loss of ellipticity. These

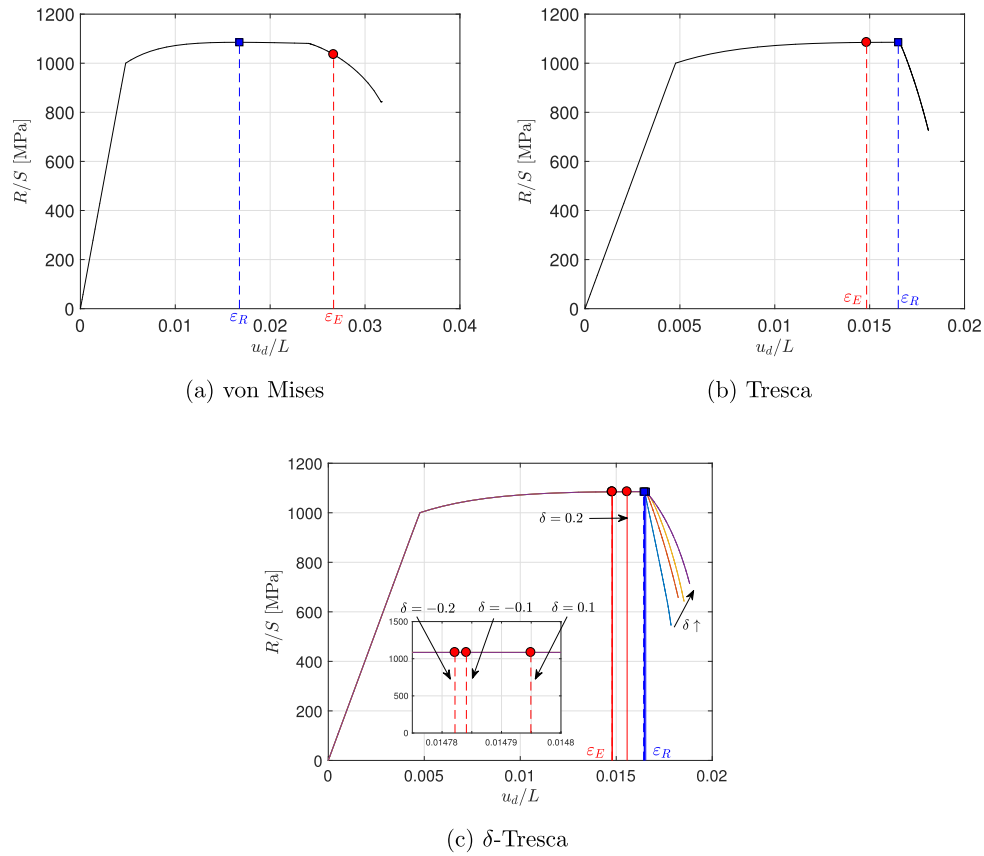


Fig. 11. Tension of a thin plate: graphs of the force resultant R/S with respect to the prescribed deformation u_d/L . The prescribed deformations ϵ_E and ϵ_R correspond to: the first occurrence of loss of ellipticity and to when R reaches its maximum value.

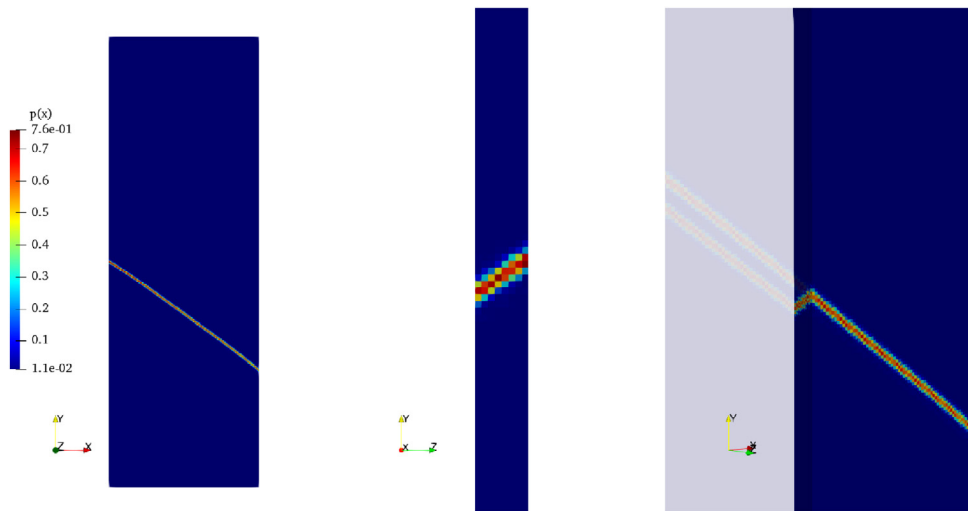


Fig. 12. Cumulative plastic strain field in a Tresca plate for $u_d/L \approx 0.0175$. Three views of the plate are shown (from left to right): front view, side view, and clipped view inside the plate.

observations are in agreement with the analysis carried out in Section 4.2.1.

5.3.2. Experimental tubular specimen undergoing simple tension

Graphs of the resultant force with respect to the prescribed displacement are shown in the right panel of Fig. 14. As in the previous examples, it can be seen that the Tresca and δ -Tresca models lose ellipticity earlier than the von Mises model. The δ -Tresca and von Mises model exhibits similar cumulative

plastic strain fields and loss of ellipticity indicators as it can be seen in Fig. 16. The Tresca test tube plastifies in a similar fashion but with different magnitudes. Note that these snapshots are taken when the structure loses ellipticity for the first time during simulation and for further time steps, the three models exhibit different localization bands. The von Mises model was expected to remain elliptic but due to the geometry, the material does not undergo simple tension, even in the region of interest.

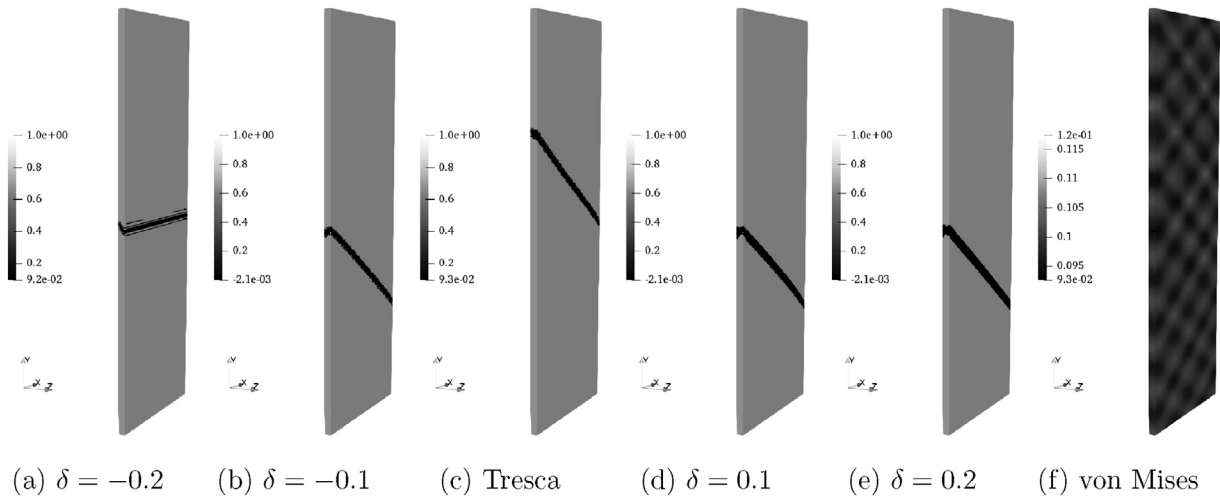


Fig. 13. Tension of a thin plate: loss of ellipticity indicators for various plastic models and a prescribed displacement $u_d/L \approx 0.0175$.

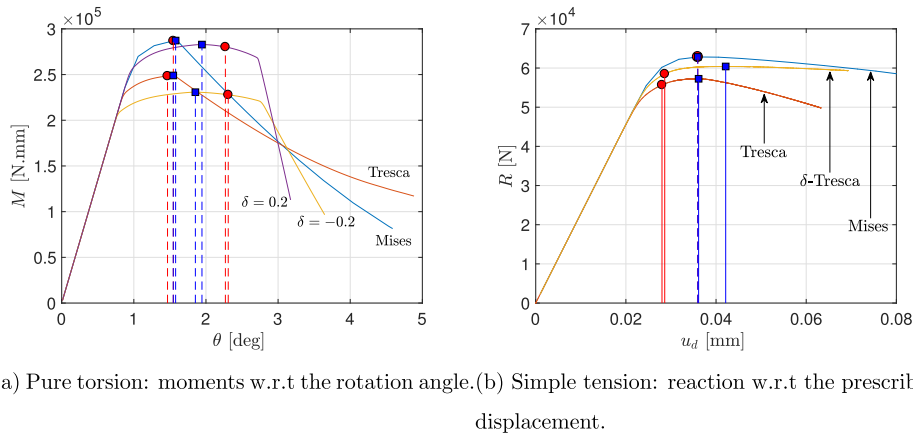


Fig. 14. Simple tension and pure torsion of a tubular specimen. Red bullets indicate loss of ellipticity and blue squares point out the maximum load. (For interpretation of the references to colour in this figure legend, the reader is referred to the web version of this article.)

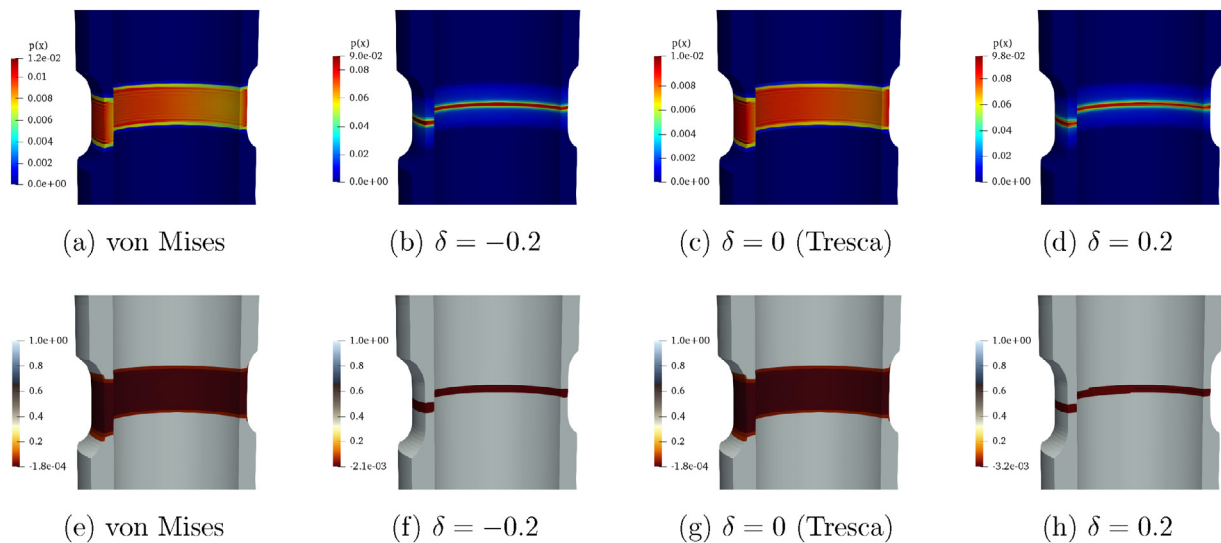


Fig. 15. Pure torsion test: cumulative plastic strain (top row) and loss of ellipticity indicator $\inf_n \det(\mathbf{Q}_{ep}(\mathbf{n}))$ (bottom row) when ellipticity is lost for the first time during the simulations (Fig. 14(a)).

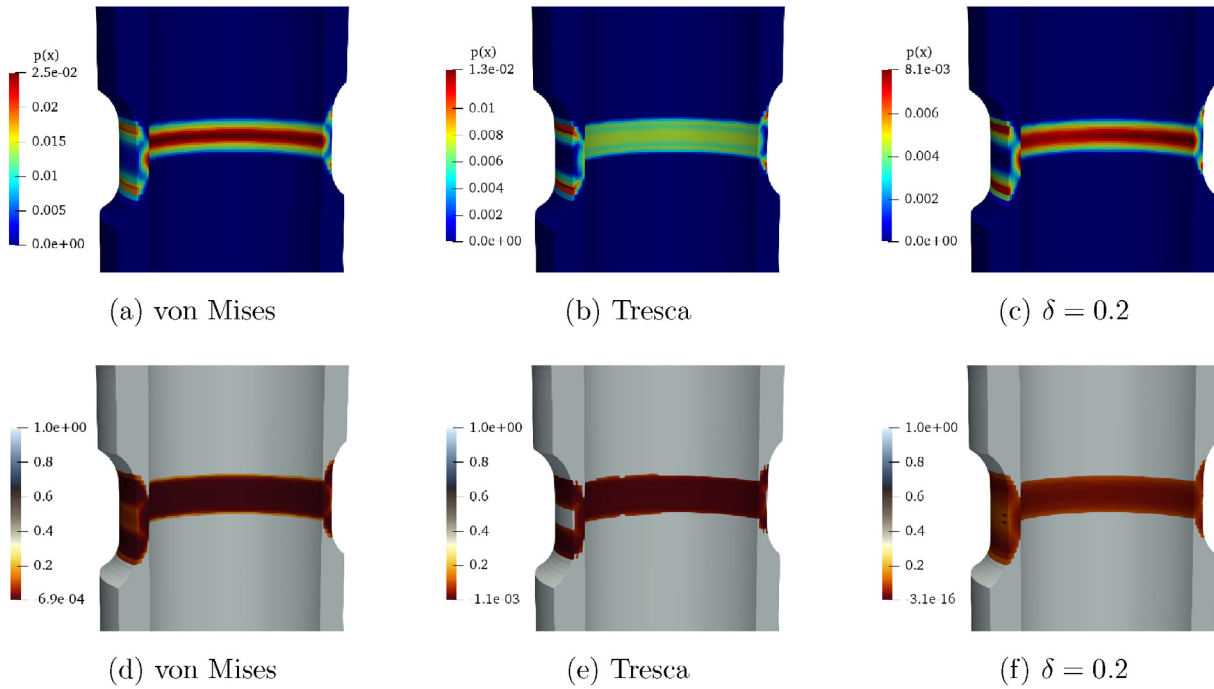


Fig. 16. Simple tension: cumulative plastic strains (top row) and loss of ellipticity indicator $\inf_n \det(\mathbf{Q}_{ep}(\mathbf{n}))$ (bottom row) when ellipticity is lost for the first time during the simulations (Fig. 14 (b)).

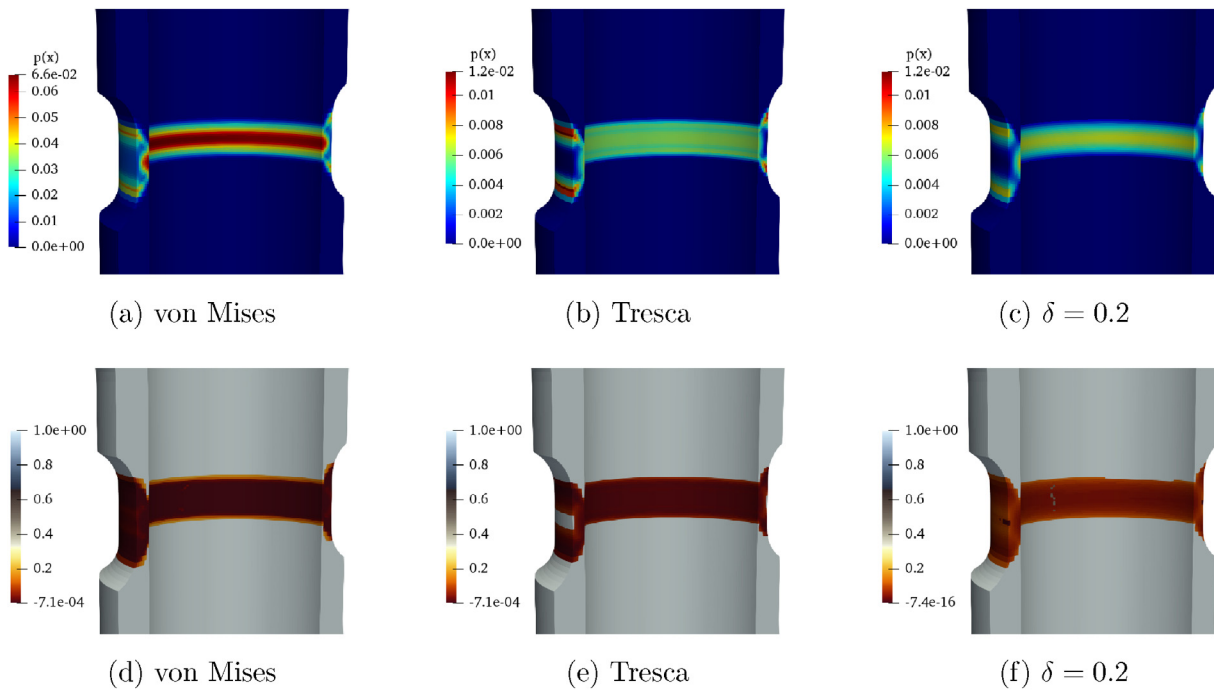


Fig. 17. Combined tension–torsion: cumulative plastic strains (top row) and loss of ellipticity indicator $\inf_n \det(\mathbf{Q}_{ep}(\mathbf{n}))$ (bottom row) when ellipticity is lost for the first time during the simulations.

5.3.3. Experimental tubular specimen undergoing combined torsion-tension

In this last scenario, a 1 mm vertical prescribed displacement and a 10° rotation along the test tube axis are applied to the top surface. Snapshots of the cumulative plastic strain fields and the

loss of ellipticity indicators are shown in Fig. 17. The von Mises model loses ellipticity for $u_d = 0.0396\text{mm}$ and $\theta = 0.396^\circ$, while the Tresca and δ -Tresca model lose ellipticity at times for $u_d = 0.0275\text{mm}$, $\theta = 0.275^\circ$, and $u_d = 0.0275\text{mm}$, $\theta = 0.273^\circ$, respectively. Each model exhibit similar localization patterns but

with different magnitudes. While the von Mises model tends to localize on the inner surface of the specimen, the Tresca model localizes on the outer surface. The δ -Tresca seems to stabilize the simulation as it leads to lower cumulative plastic strains when ellipticity is lost.

6. Conclusion

This work is concerned with the analysis of ellipticity when dealing with non-smooth yield surfaces. Towards this end, we consider a class of yield functions that are given by a linear combination of the principal stresses. In principal stress space, yield functions belonging to such a family are non-smooth as they include two sharp corners on their surfaces, referred to as the left and right corners. For simplicity, three particular cases are considered, namely, the Tresca, δ -Tresca, and τ -Tresca models. The parameters δ and τ allow for modifying the positions and the shape of the corners. The following findings are made:

- The corners on the yield surface have a significant effect on the conditions for loss of ellipticity, *i.e.*, they strongly affect the critical hardening modulus. In order to better understand this phenomenon, two new parametric families of yield functions are introduced. The parameter δ (resp. τ) in the δ -Tresca (resp. τ -Tresca) model allows for increasing or decreasing the angle formed by the right corner (resp. left corner) of the yield surface. It is found that the presence of such corners lead to loss of ellipticity as soon as the hardening modulus vanishes.
- A numerical procedure for the detection of loss of ellipticity in multisurface plasticity is obtained by combining the recent algorithm proposed by Al Kotob et al. (2019) and the works of Petryk (2000) and Sawischlewski et al. (1996). This numerical approach is used to determine the critical hardening moduli for the considered non-smooth yield function and to detect loss of ellipticity in finite element simulations.
- An explicit expression of the subdifferential of the non-smooth yield function is derived and generalize recent expressions obtained in the cases of the Tresca (He et al., 2005) and Mohr–Coulomb (Sysala et al., 2017) models. This expression allows for expressing the flow rule in an abstract compact form and can be used for deriving an implicit integration algorithm.
- Finite element simulations on simple geometries undergoing simple tension show that the Tresca and δ -Tresca models lead to loss of ellipticity much earlier than the commonly used von Mises model. More specifically, the von Mises model loses ellipticity for unrealistic deformations that are out of the range of the small perturbations assumption. In contrast, the Tresca and δ -Tresca models may lose ellipticity for much lower deformations.
- Finite element simulations on a realistic structure show that the choice of the yield function can lead to drastic differences in terms of localization and loss of ellipticity. In all cases, it is seen that the non-smooth yield functions lose ellipticity earlier than the von Mises model and they also lead to different localization patterns and localization magnitudes.

These findings suggest that the choice of the yield function, and its smoothness, is of primary importance for structural computations. Strain localization observed in many engineering alloys (Defaïsse et al., 2018; Al Kotob et al., 2019) can lead to slant fracture that cannot be properly described by existing ductile fracture

models. The von Mises model and more generally smooth yield functions that are used in the industry, do not properly account for such localization modes under tension. We anticipate that more realistic models should incorporate corners, emerging from polycrystal plasticity. As demonstrated in the present work, such models can predict earlier strain localization events.

In future works, it is planned to study the influence of kinematic hardening on material instabilities, incorporate large deformation in the present analysis, and investigate the influence of corners in polycrystal plasticity.

Declaration of Competing Interest

The authors declare that they have no known competing financial interests or personal relationships that could have appeared to influence the work reported in this paper.

Acknowledgement

The financial support of the DGAC (Direction générale de l'Aviation civile) is gratefully acknowledged.

Appendix A. Subdifferential set for the family of yield criteria linear in principal stresses

In this section, an explicit expression of the subdifferential set $\partial\varphi$ (70) is provided for the yield function defined by Eq. (63). To the authors' best knowledge, such expressions are only available for the Tresca (He et al., 2005) and Mohr–Coulomb (Sysala et al., 2017) models. Based on the previous work of Vallée et al. (2006), two approaches are presented by He et al. (2005), namely, a direct approach that starts from the definition (70), and an indirect approach that uses corollary results of convex analysis (van Tiel, 1984; Rusczyński, 2006). In the work of Sysala et al. (2017), the expression of the subdifferential set is obtained starting from its definition (70) in the case of a Mohr–Coulomb criterion. Here, we adopt an indirect approach. The canonical yield function (63) can be rewritten as

$$\varphi(\boldsymbol{\sigma}) = (a_1 - a_2)\sigma_1(\boldsymbol{\sigma}) + a_2\text{Tr}(\boldsymbol{\sigma}) + (a_2 - a_3)(-\sigma_3(\boldsymbol{\sigma})), \quad (\text{A.1})$$

where it is recalled that $a_1 > 0, a_3 < 0, a_1 > a_2 > a_3$, and $\sigma_1(\boldsymbol{\sigma}) \geq \sigma_2(\boldsymbol{\sigma}) \geq \sigma_3(\boldsymbol{\sigma})$. According to Vallée et al. (2006) and Rusczyński, 2006, the functions $\boldsymbol{\sigma} \mapsto \sigma_1(\boldsymbol{\sigma})$ and $\boldsymbol{\sigma} \mapsto (-\sigma_3(\boldsymbol{\sigma}))$ are both convex. The yield function (A.1) being given by a sum of three convex functions, it can be deduced (van Tiel, 1984; Rusczyński, 2006) that its subdifferential takes the form

$$\partial\varphi(\boldsymbol{\sigma}) = (a_1 - a_2)\partial_{\boldsymbol{\sigma}}\sigma_1(\boldsymbol{\sigma}) + a_2\partial_{\boldsymbol{\sigma}}\text{Tr}(\boldsymbol{\sigma}) + (a_2 - a_3)\partial_{\boldsymbol{\sigma}}(-\sigma_3(\boldsymbol{\sigma})). \quad (\text{A.2})$$

The subdifferential set of the largest eigenvalue is given by (Vallée et al., 2006; Rusczyński, 2006)

$$\partial\sigma_1(\boldsymbol{\sigma}) = \left\{ \boldsymbol{\xi} = \sum_{i=1}^3 \xi_i \mathbf{m}_i \otimes \mathbf{m}_i \mid \boldsymbol{\xi} : \boldsymbol{\sigma} = \sigma_1(\boldsymbol{\sigma}), \text{Tr}(\boldsymbol{\xi}) = 1 \right\}, \quad (\text{A.3})$$

and can be reduced to

$$\partial\sigma_1(\boldsymbol{\sigma}) = \left\{ \boldsymbol{\xi} = \sum_{i=1}^3 \xi_i \mathbf{m}_i \otimes \mathbf{m}_i \mid (\sigma_1 - \sigma_2)(\xi_1 - 1) + (\sigma_2 - \sigma_3)(-\xi_3) = 0, \text{Tr}(\boldsymbol{\xi}) = 1 \right\}. \quad (\text{A.4})$$

The subdifferential of the smallest eigenvalue is such that $\partial_{\boldsymbol{\sigma}}(-\sigma_3(\boldsymbol{\sigma})) = -\partial_{\boldsymbol{\sigma}}\sigma_1(-\boldsymbol{\sigma})$. Using Eq. (A.3) and the relationship $\sigma_1(-\boldsymbol{\sigma}) = -\sigma_3(\boldsymbol{\sigma})$, it can be deduced that

$$\begin{aligned} \partial(-\sigma_3(\boldsymbol{\sigma})) = \\ \left\{ \boldsymbol{\eta} = \sum_{i=1}^3 \boldsymbol{\eta}_i \mathbf{m}_i \otimes \mathbf{m}_i \mid (\sigma_1 - \sigma_2)\boldsymbol{\eta}_1 + (\sigma_2 - \sigma_3)(-\mathbf{1} - \boldsymbol{\eta}_3) = \mathbf{0}, \text{Tr}(\boldsymbol{\eta}) = -1 \right\}. \end{aligned} \quad (\text{A.5})$$

Finally, the function $\boldsymbol{\sigma} \mapsto \text{Tr}(\boldsymbol{\sigma})$ is smooth and its subdifferential is given by the singleton $\{\mathbf{I}\}$ containing the identity tensor. It follows that any tensor $\mathbf{W} \in \partial\phi(\boldsymbol{\sigma}, R)$ is given by

$$\begin{aligned} \mathbf{W} = (a_1 - a_2)\boldsymbol{\xi} + a_2 \sum_{i=1}^3 \mathbf{m}_i \otimes \mathbf{m}_i + (a_2 - a_3)\boldsymbol{\eta}, \quad \boldsymbol{\xi} \\ \in \partial\sigma_1(\boldsymbol{\sigma}), \quad \boldsymbol{\eta} \in \partial(-\sigma_3(\boldsymbol{\sigma})). \end{aligned} \quad (\text{A.6})$$

A compact expression of the subdifferential set can be obtained by noticing that the coefficients W_1, W_2, W_3 such that $\mathbf{W} = \sum_{i=1}^3 W_i \mathbf{m}_i \otimes \mathbf{m}_i$ satisfy

$$\begin{aligned} (\sigma_1 - \sigma_2)(W_1 - a_1) + (\sigma_2 - \sigma_3)(a_3 - W_3) \\ = 0, \quad W_1 + W_2 + W_3 = a_1 + a_2 + a_3. \end{aligned} \quad (\text{A.7})$$

Hence, Eq. (A.2) is also given by

$$\begin{aligned} \partial\phi(\boldsymbol{\sigma}) \\ = \left\{ \mathbf{N} = \sum_{i=1}^3 N_i \mathbf{m}_i \otimes \mathbf{m}_i \mid (\sigma_1 - \sigma_2)(N_1 - a_1) + (\sigma_2 - \sigma_3)(a_3 - N_3) = 0, \text{Tr}(\mathbf{N}) = \sum_{i=1}^3 a_i \right\}. \end{aligned} \quad (\text{A.8})$$

Using either Eq. (A.2) or Eq. (A.8) and by considering stress tensors on the smooth portion, left corner, or right corner of the yield surface, it can be verified that the abstract flow rule $\dot{\boldsymbol{\epsilon}}^p \in \dot{\gamma} \partial\phi(\boldsymbol{\sigma})$ is equivalent to the multisurface flow rule presented in B.

Appendix B. Multisurface flow rule

We propose to deduce the multisurface form of the flow rule $\dot{\boldsymbol{\epsilon}}^p = \sum_{j \in \mathcal{J}} \dot{\gamma}_j \mathbf{N}_j$ (see Section 4.1) from the subdifferential-based flow rule $\dot{\boldsymbol{\epsilon}}^p \in \dot{\gamma} \partial\phi(\boldsymbol{\sigma})$ (see Eq. (69)). Following Section 2.2, we let μ_1, μ_2, μ_3 be three positive real numbers, and we introduce the auxiliary yield function $\tilde{\varphi}$ defined as

$$\tilde{\varphi}(\boldsymbol{\sigma}) = \mu_1 \varphi_1(\boldsymbol{\sigma}) + \mu_2 \varphi_2(\boldsymbol{\sigma}) + \mu_3 \varphi_3(\boldsymbol{\sigma}). \quad (\text{B.1})$$

In order to determine possible sets of values for μ_1, μ_2, μ_3 such that $\tilde{\varphi}(\boldsymbol{\sigma}) = \varphi(\boldsymbol{\sigma})$, four cases have to be distinguished depending on the current values of the principal stresses:

- (a) If $\boldsymbol{\sigma}$ lies in the interior of the elastic domain, then $\tilde{\varphi}(\boldsymbol{\sigma}) < R$ regardless of the values of μ_1, μ_2 , and μ_3 .
- (b) If $\boldsymbol{\sigma} \in \partial\mathbb{E}_s$, then $\varphi_1(\boldsymbol{\sigma}) = R$. Hence, it can be deduced that $\varphi(\boldsymbol{\sigma}) = \tilde{\varphi}(\boldsymbol{\sigma})$ for $\mu_1 = 1, \mu_2 = 0$, and $\mu_3 = 0$. It follows that the subdifferential set $\partial\varphi$ is given by

$$\partial\varphi(\boldsymbol{\sigma}) = \partial\varphi_1(\boldsymbol{\sigma}), \quad (\text{B.2})$$

and thus $\dot{\boldsymbol{\epsilon}}^p = \mu_1 \dot{\gamma} \partial\varphi_1(\boldsymbol{\sigma})$. Given that the mapping $\boldsymbol{\sigma} \mapsto \varphi_1(\boldsymbol{\sigma}, \cdot)$ is differentiable, the set $\partial\varphi_1(\boldsymbol{\sigma})$ reduces to the singleton $\{\mathbf{N}_1\}$. Based on this result, the flow rule takes the form

$$\dot{\boldsymbol{\epsilon}}^p = \dot{\gamma}_1 \mathbf{N}_1, \quad \dot{\gamma}_1 \equiv \dot{\gamma}. \quad (\text{B.3})$$

- (c) If $\boldsymbol{\sigma} \in \partial\mathbb{E}_l$, then $\varphi_1(\boldsymbol{\sigma}) = R$ and $\varphi_2(\boldsymbol{\sigma}) = R$. It follows that $\varphi(\boldsymbol{\sigma}) = \tilde{\varphi}(\boldsymbol{\sigma})$ for $\mu_1 \geq 0$ and $\mu_2 \geq 0$ such that $m_1 + m_2 = 1$, and $\mu_3 = 0$. In this case, the subdifferential set $\partial\varphi$ can also be written as

$$\partial\varphi(\boldsymbol{\sigma}) = \mu_1 \partial\varphi_1(\boldsymbol{\sigma}) + \mu_2 \partial\varphi_2(\boldsymbol{\sigma}), \quad \mu_1 + \mu_2 = 1. \quad (\text{B.4})$$

Hence, it can be deduced that the flow rule takes the form

$$\dot{\boldsymbol{\epsilon}}^p = \dot{\gamma}_1 \mathbf{N}_1 + \dot{\gamma}_2 \mathbf{N}_2, \quad \dot{\gamma}_1 \equiv \mu_1 \dot{\gamma}, \quad \dot{\gamma}_2 \equiv \mu_2 \dot{\gamma}, \quad (\text{B.5})$$

with

$$\dot{\gamma} = \dot{\gamma}_1 + \dot{\gamma}_2.$$

- (d) Finally, if $\boldsymbol{\sigma} \in \partial\mathbb{E}_r$, one has $\varphi_1(\boldsymbol{\sigma}) = R$ and $\varphi_3(\boldsymbol{\sigma}) = R$. Hence, $\varphi(\boldsymbol{\sigma}) = \tilde{\varphi}(\boldsymbol{\sigma})$ for any $\mu_1 \geq 0$ and $\mu_3 \geq 0$ such that $\mu_1 + \mu_3 = 1$, and $\mu_2 = 0$. The subdifferential set $\partial\varphi$ can be additively decomposed as

$$\partial\varphi(\boldsymbol{\sigma}) = \mu_1 \partial\varphi_1(\boldsymbol{\sigma}) + \mu_3 \partial\varphi_3(\boldsymbol{\sigma}), \quad \mu_1 + \mu_3 = 1, \quad (\text{B.6})$$

where $\partial\varphi_3 = \{\mathbf{N}_3\}$. The flow rule $\dot{\boldsymbol{\epsilon}}^p \in \dot{\gamma} \partial\varphi$ then takes the form

$$\dot{\boldsymbol{\epsilon}}^p = \dot{\gamma}_1 \mathbf{N}_1 + \dot{\gamma}_3 \mathbf{N}_3, \quad \dot{\gamma}_1 \equiv \mu_1 \dot{\gamma}, \quad \dot{\gamma}_3 \equiv \mu_3 \dot{\gamma}, \quad (\text{B.7})$$

with

$$\dot{\gamma} = \dot{\gamma}_1 + \dot{\gamma}_3.$$

In summary, the flow rule can equivalently be written as

$$\dot{\boldsymbol{\epsilon}}^p \in \dot{\gamma} \partial\phi(\boldsymbol{\sigma}),$$

and

$$\dot{\boldsymbol{\epsilon}}^p = \sum_{j \in \mathcal{J}} \dot{\gamma}_j \mathbf{N}_j, \quad \dot{\gamma}_j = \dot{\gamma} \mu_j, \quad \sum_{j \in \mathcal{J}} \mu_j = 1.$$

As a result, it is always possible to find a triplet (μ_1, μ_2, μ_3) of positive scalars such that $\varphi(\boldsymbol{\sigma}) = \sum_{j=1}^3 \mu_j \varphi_j(\boldsymbol{\sigma})$ for all $\boldsymbol{\sigma} \in \mathbb{M}_s^3$. It can also be seen that this result leads to an equivalence between the abstract flow rule given by Eq. (9) and the multisurface flow rule given by Eq. (15). One advantage of the subdifferential-based flow rule is that it can lead to a simpler fully implicit integration scheme as shown by Sysala et al. (2016) for Mohr–Coulomb plasticity. It should be emphasized that for $a_1 = 1, a_2 = 0$, and $a_3 = -1$, the multisurface and subdifferential flow rule of the Tresca yield function are recovered (de Souza Neto et al., 2011; He et al., 2005).

Appendix C. Explicit expressions of the critical hardening moduli in the case of two active mechanisms

This appendix summarizes explicit expressions of critical hardening moduli obtained by Sawischlewski et al. (1996) for a family of matrices $[H(\ell)]$ given by

$$[H(\ell)] \equiv H_\ell(\ell[i_m] + (1 - \ell)[1]), \quad (\text{C.1})$$

where H_ℓ is a scalar hardening modulus and $[i_m]_{\ell} = 1$ for all $I, J \in \{1, \dots, M_{\text{act}}\}^2$. These results are valid in the simplest case of two active mechanisms. Three cases can be distinguished.43

- (b) For $\ell = 0$, it is found that

$$H_0^2 - H_0 \text{adj}([\pi(\mathbf{n})] - [\chi]) : [1] + \det([\pi(\mathbf{n})] - [\chi]) = 0, \quad (\text{C.4})$$

which corresponds to the characteristic equation for $[\pi(\cdot)] - [\chi]$ with H_0 as an eigenvalue. Hence, the critical hardening modulus is given by

$$H_0^{\text{crit}} = \max_{\|\mathbf{n}\|=1} \max_K \lambda_K([\pi(\mathbf{n})] - [\chi]). \quad (\text{C.5})$$

- (c) For an arbitrary ℓ such that $\ell \neq 0$ and $\ell \neq 1$, one has

$$a_\ell H_\ell^2 + b_\ell(\mathbf{n}) H_\ell + c(\mathbf{n}) = 0, \quad (\text{C.6})$$

where $a_\ell = (1 - \ell^2)$, $c(\mathbf{n}) = \det([\pi(\mathbf{n})] - [\chi])$, and

$$\begin{aligned} b_\ell(\mathbf{n}) = \ell \text{adj}([\pi(\mathbf{n})] - [\chi]) \\ : [i_m] + (1 - \ell) \text{adj}([\pi(\mathbf{n})] - [\chi]) : [1]. \end{aligned} \quad (\text{C.7})$$

Given a normal \mathbf{n} , the above second-order equation can easily be solved for the hardening modulus, yielding $\mathbf{n} \mapsto H_\ell(\mathbf{n})$, in order to deduce the critical hardening modulus $H_\ell^{\text{crit}} = \max_{\|\mathbf{n}\|=1} H_\ell(\mathbf{n})$. Different cases have to be distinguished depending on the value of the parameter ℓ .

Appendix D. Implicit integration scheme

The elasto-plastic constitutive problem is solved with an implicit integration scheme. A general implicit integration scheme for multisurface plasticity has been proposed by Simo et al. (1988) and recently reformulated in principal stress space by Karaulanis (2013). It should be noted that there also exist fully implicit integration schemes for the Tresca criterion with isotropic hardening (Perić and de Souza Neto, 1999; Sysala et al., 2016) and for the yield function given by Eq. (63) (Larsson and Runesson, 1996). Herein, we have recourse to the general procedure described by Simo et al. (1988) in order to easily accommodate any yield function expressed in terms of principal stresses. At a fixed Gauss point, given $\boldsymbol{\varepsilon}_n^e, p_n$, and $\Delta\boldsymbol{\varepsilon}_{n+1}$ at a given time increment t_n , we seek the updated tensor $\boldsymbol{\varepsilon}_{n+1}^e$ and the increments of the Lagrange multipliers $\Delta\gamma_{j,n+1}$ for $j = 1, \dots, m$. A sketch of the algorithm is given in the box Algorithm 1. It consists in solving the residual equation $\mathbf{r} \equiv (\mathbf{r}^e, \mathbf{r}^\phi) = \mathbf{0}$ for the principal stresses $\hat{\boldsymbol{\sigma}}_{n+1}$, the internal variable p_{n+1} , and the set of Lagrange multipliers $\{\Delta\gamma_{j,n+1}\}_{j \in \mathbb{J}}$ where

$$\begin{aligned} \mathbf{r}^e &= [C]^{-1}(\hat{\boldsymbol{\sigma}}_{n+1} - \hat{\boldsymbol{\sigma}}_{n+1}^{\text{trial}}) + \sum_{j \in \mathbb{J}} \Delta\gamma_{j,n+1} \hat{\mathbf{n}}_j, \quad \mathbf{r}_j^\phi \\ &= \phi_j(\hat{\boldsymbol{\sigma}}_{n+1}, R_{n+1}), \quad j \in \mathbb{J}, \end{aligned} \quad (\text{D.1})$$

where

- the vectors gathering the ordered principal stresses and elastic strains are related by $\hat{\boldsymbol{\sigma}}_{n+1} = [C]\hat{\boldsymbol{\varepsilon}}_{n+1}$, in which the matrix $[C]$ can easily be deduced from the entries of the fourth-order elasticity tensor \mathbb{C} ;
- the updated yield stress is given by $R_{n+1} = R(p_n + \sum_{j \in \mathbb{J}} \Delta\gamma_{j,n+1})$;
- the yield function has been written in terms of the principal stresses, i.e.,

$$\hat{\phi}_j(\hat{\boldsymbol{\sigma}}, r) = \phi_j\left(\sum_{i=1}^3 \hat{\sigma}_i \mathbf{M}_i, r\right), \quad j = 1, \dots, m, \quad (\text{D.2})$$

for any yield stress r , where $\mathbf{M}_i, i = 1, 2, 3$, denotes the elements of the eigenbasis of the stress tensor,

- and the vectors $\hat{\mathbf{n}}_1, \hat{\mathbf{n}}_2$ and $\hat{\mathbf{n}}_3$ correspond to the first-order partial derivatives of the yield function with respect to the ordered principal stresses, i.e.,

$$\hat{\mathbf{n}}_1 = \begin{bmatrix} a_1 \\ a_2 \\ a_3 \end{bmatrix}_{(\mathbf{e}_i)_{i=1}^3}, \quad \hat{\mathbf{n}}_2 = \begin{bmatrix} a_2 \\ a_1 \\ a_3 \end{bmatrix}_{(\mathbf{e}_i)_{i=1}^3}, \quad \hat{\mathbf{n}}_3 = \begin{bmatrix} a_1 \\ a_3 \\ a_2 \end{bmatrix}_{(\mathbf{e}_i)_{i=1}^3}. \quad (\text{D.3})$$

By having recourse to a Newton–Raphson procedure, one has to solve the following sequence until convergence has been met:

$$\begin{aligned} k \geq 0: \quad & [J(\boldsymbol{\eta}^{(k)})](\boldsymbol{\eta}^{(k+1)} - \boldsymbol{\eta}^{(k)}) = -\mathbf{r}(\boldsymbol{\eta}^{(k)}), \quad \boldsymbol{\eta}^{(k)} \\ & \equiv \left(\hat{\boldsymbol{\sigma}}_{n+1}^{(k)}, \boldsymbol{\alpha}_{n+1}^{(k)}, \left(\Delta\gamma_{j,n+1}^{(k)} \right)_{j \in \mathbb{J}} \right), \end{aligned} \quad (\text{D.4})$$

where $[J(\boldsymbol{\eta}^{(k)})]$ denotes the jacobian matrix for a given value $\boldsymbol{\eta}^{(k)}$ of the unknowns. The jacobian matrix is populated by the partial

derivatives of the residuals \mathbf{r}^e and \mathbf{r}^ϕ with respect to $\hat{\boldsymbol{\sigma}}_{n+1}^{(k)}, p_{n+1}^{(k)}$, and $\left(\Delta\gamma_{j,n+1}^{(k)} \right)_{j \in \mathbb{J}}$. In addition, the consistent tangent matrix that is necessary for the global Newton–Raphson scheme (at the structural level) is computed using the systematic approach presented by, e.g., Borja et al. (2003). Once the Newton–Raphson procedure has converged for some k^* , the Jacobian matrix $[J(\boldsymbol{\eta}^{(k^*)})]$ is assembled for the solution $\boldsymbol{\eta}^{(k^*)}$. The consistent tangent matrix is then given by the first (6×6) block of the inverse of the jacobian matrix $[J(\boldsymbol{\eta}^{(k^*)})]^{-1}$.

Algorithm 1: Implicit integration scheme

- 1 Compute the elastic predictor $\boldsymbol{\sigma}_{n+1}^{\text{trial}} = \mathbb{C} : (\boldsymbol{\varepsilon}_n^e + \Delta\boldsymbol{\varepsilon}_{n+1})$ and $R_{n+1}^{\text{trial}} = R(\boldsymbol{\sigma}_{n+1}^{\text{trial}})$
- 2 Compute the trial principal stresses $\hat{\boldsymbol{\sigma}}_{n+1}^{\text{trial}}$ and eigenbases $\{\mathbf{M}_i\}_{i=1}^3$ such $\boldsymbol{\sigma}_{n+1}^{\text{trial}} = \sum_{i=1}^3 \hat{\sigma}_{i,n+1}^{\text{trial}} \mathbf{M}_i$
- 3 Compute the trial yield functions $\hat{\phi}_j^{\text{trial}} = \hat{\phi}_j(\hat{\boldsymbol{\sigma}}_{n+1}^{\text{trial}}, R_{n+1}^{\text{trial}})$ for all $j = 1, \dots, m$
- 4 Compute the set of active yield surfaces $\mathbb{J} = \{j \in \{1, \dots, m\} \mid \hat{\phi}_j^{\text{trial}} > 0\}$
- 5 if $\mathbb{J} = \emptyset$ then
- 6 $\left[\begin{array}{l} \boldsymbol{\sigma}_{n+1} = \boldsymbol{\sigma}_{n+1}^{\text{trial}}, p_{n+1} = p_n \text{ and } \Delta\gamma_{j,n+1} = 0 \text{ for all } j \in \{1, \dots, m\}. \end{array} \right.$
- 7 else
- 8 $\left[\begin{array}{l} \text{Solve the residual equation } \mathbf{r} = \mathbf{0} \text{ for the principal stresses } \hat{\boldsymbol{\sigma}}_{n+1}, \text{ the} \\ \text{variable } p_{n+1}, \text{ and the set of Lagrange multipliers } \{\Delta\gamma_{j,n+1}\}_{j \in \mathbb{J}}. \end{array} \right.$
- 9 if $\Delta\gamma_{K,n+1} \leq 0$ for any $K \in \mathbb{J}$ then
- 10 $\left[\begin{array}{l} \text{Remove } K \text{ from } \mathbb{J}. \end{array} \right.$
- 11 $\left[\begin{array}{l} \text{Return to 7.} \end{array} \right.$
- 12 else
- 13 $\left[\begin{array}{l} \text{Update the stress tensor as follows: } \boldsymbol{\sigma}_{n+1} = \sum_{i=1}^3 \hat{\sigma}_{i,n+1} \mathbf{M}_i. \end{array} \right.$

References

- Al Kotob, M., Combescure, C., Mazière, M., Rose, T., Forest, S., 2019. A general and efficient multi-start algorithm for the detection of loss of ellipticity in elastoplastic structures. *Int. J. Numer. Methods Eng.* 121, 842–866.
- Benallal, A., Berstad, T., Børvik, T., Hopperstad, O., 2010. Uniqueness, loss of ellipticity and localization for the time-discretized, rate-dependent boundary value problem with softening. *Int. J. Numer. Methods Eng.* 84, 864–882.
- Besson, J., Cailletaud, G., Chaboche, J.L., Forest, S., 2009. *Non-linear Mech. Mater.*, volume 167. Springer Science & Business Media.
- Bigoni, D., 2012. *Nonlinear solid mechanics: bifurcation theory and material instability*. Cambridge University Press.
- Bigoni, D., Hueckel, T., 1991. Uniqueness and localization-I. associative and non-associative elastoplasticity. *Int. J. Solids Struct.* 28, 197–213.
- Borja, R., Sama, K., Sanz, P., 2003. On the numerical integration of three-invariant elastoplastic constitutive models. *Comput. Methods Appl. Mech. Eng.* 192, 1227–1258.
- Cailletaud, G., 1992. A micromechanical approach to inelastic behaviour of metals. *Int. J. Plast.* 8, 55–73.
- Carstensen, C., Hackl, K., Mielke, A., 2001. Non-convex potentials and microstructures in finite-strain plasticity. *Proceedings of the royal society of London. Series A: mathematical, physical and engineering sciences* 458, 299–317..
- Chambon, R., Crochepeyre, S., Desrues, J., 2000. Localization criteria for non-linear constitutive equations of geomaterials. *Mech. Cohes. Friction. Mater.* 5, 61–82.
- Christoffersen, J., Hutchinson, J., 1979. A class of phenomenological corner theories of plasticity. *J. Mech. Phys. Solids* 27, 465–487.
- Clarke, F., 1990. *Optim. Nonsmooth Anal.*, volume 5. SIAM, New-York.
- Dafaisse, C., Mazière, M., Marcin, L., Besson, J., 2018. Ductile fracture of an ultra-high strength steel under low to moderate stress triaxiality. *Eng. Fract. Mech.* 194, 301–318.

- Eve, R., Gültop, T., Reddy, B., 1990. An internal variable finite-strain theory of plasticity within the framework of convex analysis. *Q. Appl. Math.* 48, 625–643.
- Eve, R., Reddy, B., Rockafellar, R., 1990. An internal variable theory of elastoplasticity based on the maximum plastic work inequality. *Q. Appl. Math.* 48, 59–83.
- Han, W., Reddy, B., 2012. *Plasticity: mathematical theory and numerical analysis*, 9. Springer Science & Business Media.
- He, Q.C., Vallée, C., Lerintiu, C., 2005. Explicit expressions for the plastic normality-flow rule associated to the Tresca yield criterion. *Z. Angew. Math. Phys. ZAMP* 56, 357–366.
- Hill, R., 1962. Acceleration waves in solids. *J. Mech. Phys. Solids* 10, 1–16.
- Hughes, T., Shakib, F., 1986. Pseudo-corner theory: A simple enhancement of J2-flow theory for applications involving non-proportional loading. *Eng. Comput.* 3, 116–120.
- Hutchinson, J., Tvergaard, V., 1980. Surface instabilities on statically strained plastic solids. *Int. J. Mech. Sci.* 22, 339–354.
- Hutchinson, J., Tvergaard, V., 1981. Shear band formation in plane strain. *Int. J. Solids Struct.* 17, 451–470.
- Karaoulanis, F., 2013. Implicit numerical integration of nonsmooth multisurface yield criteria in the principal stress space. *Arch. Comput. Methods Eng.* 20, 263–308.
- Koiter, W., 1953. Stress-strain relations, uniqueness and variational theorems for elastic-plastic materials with a singular yield surface. *Q. Appl. Math.* 11, 350–354.
- Kuroda, M., 2015. A higher-order strain gradient plasticity theory with a corner-like effect. *Int. J. Solids Struct.* 58, 62–72.
- Kuroda, M., 2016. A strain-gradient plasticity theory with a corner-like effect: a thermodynamics-based extension. *Int. J. Fract.* 200, 115–125.
- Kuroda, M., Tvergaard, V., 2001. A phenomenological plasticity model with non-normality effects representing observations in crystal plasticity. *J. Mech. Phys. Solids* 49, 1239–1263.
- Larsson, R., Runesson, K., 1996. Implicit integration and consistent linearization for yield criteria of the Mohr-Coulomb type. *Mech. Cohes. Friction. Mater.* 1, 367–383.
- Mandel, J., 1965. Généralisation de la théorie de plasticité de W.T. Koiter. *Int. J. Solids Struct.* 1, 273–295.
- Mielke, A., 2004. Existence of minimizers in incremental elasto-plasticity with finite strains. *SIAM J. Math. Anal.* 36, 384–404.
- Moreau, J.J., 1976. Application of convex analysis to the treatment of elastoplastic systems. In: *Appl. Methods Funct. Anal. Probl. Mech.*. Springer, pp. 56–89.
- Mosler, J., 2005. Numerical analyses of discontinuous material bifurcation: Strong and weak discontinuities. *Comput. Methods Appl. Mech. Eng.* 194, 979–1000.
- Nguyen, Q., 2000. *Stability and nonlinear solid mechanics*. Wiley.
- Perić, D., de Souza Neto, E., 1999. A new computational model for Tresca plasticity at finite strains with an optimal parametrization in the principal space. *Comput. Methods Appl. Mech. Eng.* 171, 463–489.
- Petryk, H., 1992. Material instability and strain-rate discontinuities in incrementally nonlinear continua. *J. Mech. Phys. Solids* 40, 1227–1250.
- Petryk, H., 2000. General conditions for uniqueness in materials with multiple mechanisms of inelastic deformation. *J. Mech. Phys. Solids* 48, 367–396.
- Petryk, H., 2014. *Mat. Instab. Elastic Plastic Solids*, volume 414. Springer.
- Petryk, H., Thermann, K., 1992. On discretized plasticity problems with bifurcations. *Int. J. Solids Struct.* 29, 745–765.
- Petryk, H., Thermann, K., 2002. Post-critical plastic deformation in incrementally nonlinear materials. *J. Mech. Phys. Solids* 50, 925–954.
- Pilvin, P., 1994. The contribution of micromechanical approaches to the modelling of inelastic behaviour. In: Pineau, A., Cailletaud, G., Lindley, T. (Eds.), *4th International Conference on Biaxial/multiaxial Fatigue*. Saint-Germain, France, ESIS, pp. 31–46.
- Reddy, B., 2017. *Mathematical Foundations of Elastoplastic Deformations in Solids*. American Cancer Society, *Encyclopedia of Computational Mechanics Second Edition*.
- Rice, J., 1976. The localization of plastic deformation, in: W.T. Koiter (Ed.), *Theoretical and Applied Mechanics*, North-Holland Publishing Company. pp. 207–220.
- Rønning, L., Hopperstad, O., Larsen, P., 2010. Numerical study of the effects of constitutive models on plastic buckling of plate elements. *Eur. J. Mech.-A/Solids* 29, 508–522.
- Ruszczynski, A., 2006. *Nonlinear Optimization*. Princeton University Press.
- Sawischlewski, E., Steinmann, P., Stein, E., 1996. Modelling and computation of instability phenomena in multisurface elasto-plasticity. *Comput. Mech.* 18, 245–258.
- Simo, J., 1987. A J2-flow theory exhibiting a corner-like effect and suitable for large-scale computation. *Comput. Methods Appl. Mech. Eng.* 62, 169–194.
- Simo, J., Hughes, T., 2006. *Computational inelasticity*. volume 7 of *Interdisciplinary Applied Mathematics*. Springer Science & Business Media.
- Simo, J., Kennedy, J., Govindjee, S., 1988. Non-smooth multisurface plasticity and viscoplasticity. loading/unloading conditions and numerical algorithms. *Int. J. Numer. Methods Eng.* 26, 2161–2185.
- de Souza Neto, E., Peric, D., Owen, D., 2011. *Computational methods for plasticity: theory and applications*. John Wiley & Sons.
- Stein, E., Steinmann, P., Miehe, C., 1995. Instability phenomena in plasticity: modelling and computation. *Comput. Mech.* 17, 74–87.
- Steinmann, P., 1996. On localization analysis in multisurface hyperelasto-plasticity. *J. Mech. Phys. Solids* 44, 1691–1713.
- Suquet, P., 1981. Sur les équations de la plasticité: existence et régularité des solutions. *J. Méc.* 20, 3–39.
- Sysala, S., Čermák, M., Koudelka, T., Kruis, J., Zeman, J., Blaheta, R., 2016. Subdifferential-based implicit return-mapping operators in computational plasticity. *ZAMM Z. Angew. Math. Mech.* 96, 1318–1338.
- Sysala, S., Čermák, M., Ligurský, T., 2017. Subdifferential-based implicit return-mapping operators in Mohr-Coulomb plasticity. *ZAMM Z. Angew. Math. Mech.* 97, 1502–1523.
- van Tiel, J., 1984. *Convex analysis*. John Wiley.
- Triantafyllidis, N., Needleman, A., Tvergaard, V., 1982. On the development of shear bands in pure bending. *Int. J. Solids Struct.* 18, 121–138.
- Tvergaard, V., Needleman, A., Lo, K., 1981. Flow localization in the plane strain tensile test. *J. Mech. Phys. Solids* 29, 115–142.
- Vallée, C., He, Q.C., Lerintiu, C., 2006. Convex analysis of the eigenvalues of a 3d second-order symmetric tensor. *J. Elastic.* 83, 191–204.
- Yu, M., 1983. Twin shear stress yield criterion. *Int. J. Mech. Sci.* 25, 71–74.
- Zhang, S., Jiang, X., Xiang, C., Deng, L., Li, Y., 2020. Proposal and application of a new yield criterion for metal plastic deformation. *Arch. Appl. Mech.* 90, 1705–1722.